On the momentum flux of vertically-propagating orographic gravity waves excited in nonhydrostatic flow over three-dimensional orography

Article

Accepted Version

On the Momentum Flux of Vertically-Propagating Orographic Gravity Waves Excited in Nonhydrostatic Flow over Three-dimensional Orography

Xin Xu[1], Runqiu Li[1], Miguel A. C. Teixeira[2], Yixiong Lu[3]

[1]*Key Laboratory of Mesoscale Severe Weather/Ministry of Education, and School of Atmospheric Sciences, Nanjing University, Nanjing 210023, Jiangsu, P. R. China*
[2]*University of Reading, Department of Meteorology, Meteorology Building, Whiteknights Road, Earley Gate, Reading RG6 6ET, UK*
[3]*Beijing Climate Center, China Meteorological Administration, Beijing 100081, P. R. China*

Submitted to *Journal of the Atmospheric Sciences*
8th December 2020

Corresponding to: Xin Xu (xinxu@nju.edu.cn)

School of Atmospheric Sciences, Nanjing University
No. 163, Xianlin Avenue, Nanjing, Jiangsu, 210023, P. R. China

Abstract

This work studies nonhydrostatic effects (NHE) on the momentum flux of orographic gravity waves (OGWs) forced by isolated three-dimensional orography. Based on linear wave theory, an asymptotic expression for low horizonal Froude number ($Fr = \frac{\sqrt{U^2+(\gamma V)^2}}{Na}$ where (U, V) is the mean horizontal wind, γ and a are the orography anisotropy and half-width and N is the buoyancy frequency) is derived for the gravity wave momentum flux (GWMF) of vertically-propagating waves. According to this asymptotic solution, which is quite accurate for any value of Fr, NHE can be divided into two terms (NHE1 and NHE2). The first term contains the high-frequency parts of the wave spectrum that are often mistaken as hydrostatic waves, and only depends on Fr. The second term arises from the difference between the dispersion relationships of hydrostatic and nonhydrostatic OGWs. Having an additional dependency on the horizontal wind direction and orography anisotropy, this term can change the GWMF direction. Examination of NHE for OGWs forced by both circular and elliptical orography reveals that the GWMF is reduced as Fr increases, at a faster rate than for two-dimensional OGWs forced by a ridge. At low Fr, the GWMF reduction is mostly attributed to the NHE2 term, whereas the NHE1 term starts to dominate above about $Fr = 0.4$. The behavior of NHE is mainly determined by Fr, while horizontal wind direction and orography anisotropy play a minor role. Implications of the asymptotic GWMF expression for the parameterization of nonhydrostatic OGWs in high-resolution and/or variable-resolution models are discussed.

1 Introduction

Orographic gravity waves (OGWs) triggered by stably stratified airflow over topography have been the subject of many studies over the last century. These waves can propagate upward and thus have great importance for the large-scale circulation in the middle atmosphere (Fritts and Alexander 2003). They are also closely related to various severe weather phenomena, like clear air turbulence (CAT) and downslope windstorms occurring in the troposphere (Smith 1985). Given that their horizonal spatial scales vary from a few to hundreds of kilometers, OGWs cannot be fully resolved by numerical weather prediction (NWP) and general circulation models (GCMs). As a result, the impacts of unresolved OGWs need to be parameterized (Kim et al. 2003).

Many parameterization schemes have been developed for subgrid-scale OGWs since the 1980s (e.g., Palmer et al. 1986; McFarlane 1987; Kim and Arakawa 1995; Lott and Miller 1997; Scinocca and MacFarlane 2000; Kim and Doyle 2005), which are now routinely implemented in various operational models for both weather forecasts and climate simulations. In general, these schemes share many common assumptions, such as the columnar propagation of OGWs (Plougonven et al. 2020). They also assume that OGWs are generated in a non-rotating and hydrostatic framework. A state-of-the-art NWP model, the Integrated Forecasting System (IFS) model of the European Centre for Medium-range Weather Forecasts (ECMWF), has horizontal resolutions typically on the order of 10 km. In these circumstances, the non-rotating assumption is justified because the subgrid-scale OGWs are too short to be affected by the earth's rotation. However, this is not the case with the assumption of hydrostatic OGWs.

For small-scale OGWs with horizontal wavenumber comparable to the Scorer parameter (Scorer 1949), nonhydrostatic effects (NHE) play a key role in controlling the wave dynamics. Using the stationary phase method, Smith (1979) theoretically studied the far-field OGWs excited

by a narrow two-dimensional (2D) ridge, which are nonhydrostatic. A “dispersive tail” was found to trail downstream of the mountain, which was also revealed in a number of numerical simulations (e.g., Klemp and Durran 1983; Xue and Thorpe 1991; Zängl 2003). This suggests that the wave energy can, not only propagate upwards as in the case of hydrostatic OGWs, but also disperse downstream. Owing to nonhydrostatic dispersion, the wave activity above the mountain is weaker than in its hydrostatic counterpart, leading to a suppression of wave breaking (Zängl 2003). Nonetheless, NHE on wave breaking can be modified by the interaction between OGWs and critical levels, as studied in Guarino and Teixeira (2017) for three-dimensional (3D) OGWs excited in directional shear flows past isolated mountains. These modeling results showed that wave breaking tends to be inhibited when the background shear is weak while it is enhanced for stronger wind shear. Besides wave breaking, NHE can also influence the gravity wave momentum flux (GWMF) at the surface. The high-frequency parts of nonhydrostatic OGWs (i.e., short-wavelength components) tend to be trapped in the lower troposphere (e.g., Wurtele et al. 1996; Doyle and Durran 2002). Consequently, the GWMF associated with upward-propagating waves is smaller than that existing in the hydrostatic case (e.g., Xue et al. 2000).

The GWMF at the surface is a key parameter in the parameterization schemes of OGWs. It denotes the maximum GWMF that can be absorbed into the mean flow. Changes in the surface GWMF can affect wave breaking at high altitudes (Xu et al. 2020) and thus redistribute the wave momentum deposition, impacting the large-scale circulation in the middle atmosphere (Xu et al. 2019). However, NHE are not considered in any OGW parameterization scheme. This is mainly due to the fact that there is no analytical solution for nonhydrostatic OGWs except for very special cases. To compensate for this, some OGW parametrization schemes (e.g., Lott and Miller 1997) filter all orography of horizontal scale smaller than a few km out of the orography that serves as

input to the OGW parametrization, assuming that it only causes turbulent orographic form drag (TOFD) which is the object of a separate parametrization (e.g., Beljaars et al. 2004). However, this filtering procedure is somewhat arbitrary, ignoring the influence of the flow characteristics on how non-hydrostatic the OGWs are, and how reduced their GWMF is by NHE. In the present study, this limitation will be overcome.

Smith (1980) proposed solving the wave equation of nonhydrostatic OGWs numerically using the Fast Fourier Transform (FFT) technique, which is apparently not suitable for the purpose of OGW parameterization given its computational cost. Alternatively, ray theory has been widely adopted to obtain the asymptotic solutions of nonhydrostatic OGWs. For instance, Smith (1979) derived the far-field approximation of 2D nonhydrostatic OGWs, while Marks and Eckermann (1995) developed a ray-tracing model for 3D nonhydrostatic gravity waves in a rotating, stratified and fully compressible atmosphere. Standard ray theory often utilizes the stationary-phase method and the asymptotic solution is expressed in spatial coordinates (Shutts 1998). This spatial-ray solution is inaccurate directly over the mountain because of the presence of ray caustics there. To overcome this problem, Broutman et al. (2002) expressed the ray solution in the wavenumber rather than spatial domain, i.e., Maslov's method. This eliminates the caustics over the mountain because rays in the spectral domain are well separated. Broutman et al. (2003) further extended the so-called Fourier-ray solution to accommodate nonhydrostatic OGWs, which showed good agreement with numerical simulations. Nonetheless, the Fourier-ray solution also has caustics at the buoyancy-frequency turning point for nonhydrostatic waves. Later, Pulido and Rodas (2011) developed a higher-order ray approximation method, i.e., the Gaussian beam approximation (GBA), for OGWs generated in vertically sheared flows. In the standard ray theory, each ray only consists of a single monochromatic wavenumber (i.e., the characteristic wavenumber). On the

contrary, the GBA uses a bundle of rays centered at the characteristic wavenumber (i.e., Gaussian beams) for each ray, and considers diffractive effects. Therefore, the GBA solution is well defined even at caustics. However, all these studies focused on the wave fields rather than on the GWMF and hence OGW parameterization. Based on the GBA, Xu et al. (2017a, 2018) revised a traditional OGW parameterization scheme by explicitly incorporating the horizontal propagation (e.g., Eckermann et al. 2015; Ehard et al. 2017) and directional absorption (e.g., Shutts 1995; Xu et al. 2012; Teixeira and Miranda 2009; Teixeira and Yu 2014) of OGWs. The revised scheme was implemented into the global Weather Research and Forecasting (WRF) model, and helped improve the simulation of the stratospheric polar-night jet in the Northern Hemisphere (Xu et al. 2019).

Compared with the traditional parameterization schemes of OGWs, ray-tracing based schemes have to keep track of a number of rays, which requires a significant amount of computation (e.g., Song and Chun 2008; Amemiya and Sato 2016). This approach is thus not suitable for operational use. Teixeira et al. (2008, hereafter T08) studied the surface GWMF associated with vertically-propagating OGWs produced by nonhydrostatic and rotating flow over a 2D ridge. Instead of calculating the GWMF numerically, an asymptotic expression was derived by using Taylor expansion for weakly-nonhydrostatic and weakly-rotating conditions. Fortuitously, the asymptotic expansion was found to be fairly accurate even for nonhydrostatic inertio-gravity waves, i.e., when the nonhydrostatic or rotation effects were not weak. The analytical form of this asymptotic expression of GWMF makes it promising for practical use in OGW parameterizations in numerical models. However, T08 only considered 2D OGWs forced by a ridge, while subgrid-scale OGWs are intrinsically 3D (Lott and Miller 1997; Kim and Doyle 2005). In this work, an asymptotic expression will be derived for 3D GWMF to accommodate the parameterization of 3D

nonhydrostatic OGWs. This provides a physically-based, flow-dependent, alternative to simply filtering out the GWMF associated with waves shorter than a prescribed scale.

The rest of the paper is organized as follows. Section 2 presents the expression for surface GWMF of 3D nonhydrostatic OGWs from linear mountain wave theory. An asymptotic solution is derived in section 3 for the linear nonhydrostatic GWMF associated with vertically-propagating OGWs. The behavior of this GWMF solution is studied for both isotropic and elliptical mountains in section 4. Finally, the paper is summarized and discussed in section 5.

2 Linear theory of nonhydrostatic OGWs

In the case of steady, adiabatic, inviscid, and Boussinesq flow, the governing equation for the perturbed vertical velocity of gravity waves in spectral space is

$$\frac{\partial^2 \hat{w}}{\partial z^2} + \left[\frac{N^2K^2}{\hat{D}(z)^2} - \frac{1}{\hat{D}(z)}\frac{\partial^2 \hat{D}(z)}{\partial z^2} - K^2\right]\hat{w} = 0, \tag{1}$$

where N is the Brunt-Väisälä frequency, $K = \sqrt{k^2 + l^2}$ is the magnitude of horizontal wavenumber vector $\mathbf{K} = (k, l)$, and $\hat{D}(z) = \mathbf{V}(z) \cdot \mathbf{K} = U(z)k + V(z)l$, with $\mathbf{V}(z)$ being a horizontally uniform mean flow. The above equation is similar to Eq. (9) in Xu et al. (2012) except for the last term K^2 within the brackets, which denotes the NHE. The Earth's rotation is neglected because we only consider nonhydrostatic OGWs forced by relatively narrow orography.

In the parameterization schemes of OGWs, the mean flow is assumed to be constant when calculating the surface GWMF (e.g., Lott and Miller 1997), although vertical wind shear (either unidirectional or directional) definitely influences the GWMF (e.g., Grubišić et al. 1997; Teixeira et al. 2004; Turner et al. 2019; Xu et al. 2020). Herein, we also make this assumption, to be

consistent with existing parameterization schemes. For constant wind, i.e., $\mathbf{V}(z) = \mathbf{V_0} = (U_0, V_0)$, Eq. (1) simplifies to

$$\frac{\partial^2 \widehat{w}}{\partial z^2} + m^2 \widehat{w} = 0, \tag{2}$$

where $m^2 = \frac{N^2 K^2}{\widehat{D}_0^2} - K^2$ is the squared vertical wavenumber, and $\widehat{D}_0 = \mathbf{V_0} \cdot \mathbf{K} = U_0 k + V_0 l = |\mathbf{V_0}| K cos(\varphi - \psi_0)$, with φ and ψ_0 being the directions of $\mathbf{K}$ and $\mathbf{V_0}$ respectively. For vertically-propagating OGWs the magnitude of the horizontal wavenumber should be smaller than $\left|\frac{N}{\mathbf{V_0} \cos(\varphi - \psi_0)}\right|$. Otherwise, the vertical wavenumber will be imaginary, indicating evanescent waves that decay exponentially with height.

Under the free-slip condition at the bottom boundary, i.e., $w(z = 0) = \mathbf{V_0} \cdot \nabla h(x, y)$, the vertical velocity of upward-propagating OGWs can be determined as

$$\widehat{w}(z) = i \widehat{D}_0 \hat{h}(k, l) e^{imz}\ , \tag{3}$$

where $\hat{h}(k, l)$ is the 2D Fourier transform of the terrain elevation $h(x, y)$. In idealized studies of OGWs and their parameterizations (e.g., Phillips 1984; Lott and Miller 1997; Teixeira and Miranda 2006), elliptical bell-shaped mountains are often adopted, a convenient example of which is:

$$h(x, y) = h_0 [1 + (x/a)^2 + (y/b)^2]^{-3/2}, \tag{4}$$

where h_0 is the mountain amplitude, and a and b are the mountain half widths in the x and y directions, respectively. The horizontal aspect ratio (i.e., anisotropy) of the elliptical terrain is quantified by $\gamma = \frac{a}{b}$. The 2D Fourier transform of the terrain elevation is given by

$$\hat{h}(k, l) = \frac{h_0 ab}{2\pi} e^{-\sqrt{a^2 k^2 + b^2 l^2}} \tag{5}$$

and the GWMF at the surface is equal to

$$\boldsymbol{\tau} = -\bar{\rho}\int_{-\infty}^{+\infty}\int_{-\infty}^{+\infty}\mathbf{v}'w'dxdy. \tag{6}$$

Here $\bar{\rho}$ is the background air density, and $\mathbf{v}' = (u', v')$ and w' are the perturbed horizontal and vertical velocities in physical space, respectively. On substitution of the 2D Fourier transforms of $\mathbf{v}'$ and w' into the above equation and using the polarization relation between $\mathbf{v}'$ and w', i.e., $\hat{\mathbf{v}} = i\frac{\mathbf{K}}{K^2}\frac{\partial\hat{w}}{\partial z}$ (see the appendix of Xu et al. 2017b), one can readily obtain

$$\boldsymbol{\tau} = 4\pi^2\bar{\rho}\int_{-\infty}^{+\infty}\int_{-\infty}^{+\infty}\frac{\mathbf{K}}{K^2}\Im\left(\frac{\partial\hat{w}}{\partial z}\hat{w}^*\right)dkdl, \tag{7}$$

where $\Im(\cdot)$ denotes the imaginary part of a complex number and the asterisk indicates complex conjugate.

For the sake of computational convenience, elliptical polar coordinates are introduced, that is,

$$\tilde{k} = ak = \tilde{K}\cos\phi, \qquad \tilde{l} = bl = \tilde{K}\sin\phi. \tag{8}$$

In this situation, the terrain spectrum has a simple form that only depends on $\tilde{K}$, i.e.,

$$\hat{h}(\tilde{K}) = \frac{h_0 ab}{2\pi}e^{-\tilde{K}}. \tag{9}$$

Consequently, the GWMF can be expressed as

$$\boldsymbol{\tau} = \frac{8\pi^2\bar{\rho}}{b}\int_0^{\pi}\int_0^{\infty}(\cos\phi, \gamma\sin\phi)(\cos^2\phi + \gamma^2\sin^2\phi)^{-1}\Im\left(\frac{\partial\hat{w}}{\partial z}\hat{w}^*\right)d\tilde{K}d\phi. \tag{10}$$

Substituting Eqs. (3) and (9) into the above equation yields

$$\boldsymbol{\tau} = \Pi\int_0^{\pi}\int_0^{[Fr\cos(\phi-\chi)]^{-1}}(\cos\phi, \gamma\sin\phi)\frac{\cos(\phi-\chi)}{\sqrt{\cos^2\phi+\gamma^2\sin^2\phi}}\sqrt{1-\left[Fr\cos(\phi-\chi)\tilde{K}\right]^2}\tilde{K}^2e^{-2\tilde{K}}d\tilde{K}d\phi, \tag{11}$$

where $\Pi = 2\bar{\rho}Nh_0^2b\left|\tilde{\mathbf{V}}_0\right|$ and $\chi = \mathrm{atan}\left(\frac{\gamma V_0}{U_0}\right)$. Note that χ is the direction of $\tilde{\mathbf{V}}_0 = (U_0, \gamma V_0)$, which is similar to the actual wind $\mathbf{V_0}$ but with the y velocity component scaled by the terrain anisotropy. Only in the case of isotropic terrain (i.e., $\gamma = 1$) or when the horizontal wind is aligned

with the main axes of the orography (i.e., $U_0 = 0$ or $V_0 = 0$) is χ equal to the actual wind direction. For simplicity, it is still called the horizontal wind direction hereafter, unless otherwise stated.

The non-dimensional parameter Fr is defined as $Fr = \frac{|\widetilde{\mathbf{V}}_0|}{Na}$, which represents a measure of NHE. It is similar to the traditional Froude number ($Fr = \frac{|\mathbf{V}|}{Nh_0}$) that quantifies the nonlinearity of OGWs (e.g., Miranda and James 1992), but with the mountain amplitude replaced by the mountain width. It is thus called horizonal Froude number hereafter. Physically, the horizontal Froude number can be viewed as the ratio between the period of buoyancy oscillation ($1/N$) and the advection time of airflow past the mountain ($a/|\widetilde{\mathbf{V}}_0|$). In the limit $Fr \to 0$, i.e., slow airflow and/or a broad mountain, the OGWs are predominantly hydrostatic. As Fr increases, NHE are more and more important. In the limit $Fr \to \infty$, the airflow can quickly traverse the mountain, with no internal OGWs excited.

In Eq. (11) the upper limit of the integral over $\widetilde{K}$ is $[Fr\cos(\phi - \chi)]^{-1}$, which indicates the contribution to the GWMF coming from internal OGWs, because evanescent waves produce zero GWMF. This upper limit depends on the directions of both the mean flow and the horizontal wavenumber. To facilitate the deduction of the asymptotic GWMF expression (see section 3), this upper limit is set to Fr^{-1}, i.e.,

$$\boldsymbol{\tau}_{\text{trunc}} = \Pi \int_0^{\pi} \int_0^{Fr^{-1}} (\cos\phi, \gamma\sin\phi) \frac{\cos(\phi-\chi)}{\sqrt{\cos^2\phi+\gamma^2\sin^2\phi}} \sqrt{1 - \left[Fr\cos(\phi-\chi)\widetilde{K}\right]^2}\, \widetilde{K}^2 e^{-2\widetilde{K}} d\widetilde{K} d\phi. \tag{12}$$

This corresponds to an artificial truncation of waves with $\widetilde{K}$ between Fr^{-1} and $[Fr\cos(\phi - \chi)]^{-1}$. The latter value can go up to infinity when $\cos(\phi - \chi) \to 0$. Nonetheless, as will be shown below, these high-frequency waves only give a weak contribution to the total GWMF.

3 Asymptotic solution

Generally, a closed analytical form for Eq. (12) does not exist, and the GWMF must be evaluated by numerical integration. Yet an asymptotic solution can be derived for weakly nonhydrostatic OGWs at small Fr (see T08). In the limit $Fr \to 0$, the nonhydrostatic term in Eq. (12) can be approximated by

$$\sqrt{1-\left[Fr\cos(\phi-\chi)\widetilde{K}\right]^2} \approx 1-\frac{1}{2}Fr^2\cos^2(\phi-\chi)\widetilde{K}^2, \tag{13}$$

based upon a Taylor series expansion around $Fr = 0$ up to first order. On substitution of Eq. (13) into (12), the asymptotic GWMF ($\boldsymbol{\tau}_{asy}$) is given by the sum of $\boldsymbol{\tau}_0$, $\boldsymbol{\tau}_{asy1}$, and $\boldsymbol{\tau}_{asy2}$, as follows

$$\boldsymbol{\tau}_0 = \Pi\int_0^{\pi}(\cos\phi,\gamma\sin\phi)\frac{\cos(\phi-\chi)}{\sqrt{\cos^2\phi+\gamma^2\sin^2\phi}}\left(\int_0^{\infty}\widetilde{K}^2e^{-2\widetilde{K}}d\widetilde{K}\right)d\phi, \tag{14a}$$

$$\boldsymbol{\tau}_{asy1} = -\Pi\int_0^{\pi}(\cos\phi,\gamma\sin\phi)\frac{\cos(\phi-\chi)}{\sqrt{\cos^2\phi+\gamma^2\sin^2\phi}}\left(\int_{Fr^{-1}}^{\infty}\widetilde{K}^2e^{-2\widetilde{K}}d\widetilde{K}\right)d\phi, \tag{14b}$$

$$\boldsymbol{\tau}_{asy2} = -\frac{1}{2}Fr^2\Pi\int_0^{\pi}(\cos\phi,\gamma\sin\phi)\frac{\cos^3(\phi-\chi)}{\sqrt{\cos^2\phi+\gamma^2\sin^2\phi}}\left(\int_0^{Fr^{-1}}\widetilde{K}^4e^{-2\widetilde{K}}d\widetilde{K}\right)d\phi, \tag{14c}$$

with $\boldsymbol{\tau}_0 = \left(\tau_{0x},\tau_{0y}\right)$ denoting the GWMF of hydrostatic OGWs. In deriving these equations, we have used $\int_0^{Fr^{-1}}\widetilde{K}^2e^{-2\widetilde{K}}d\widetilde{K} = \int_0^{\infty}\widetilde{K}^2e^{-2\widetilde{K}}d\widetilde{K} - \int_{Fr^{-1}}^{\infty}\widetilde{K}^2e^{-2\widetilde{K}}d\widetilde{K}$. Using integration by parts, it is easy to show that

$$\int_0^{\infty}\widetilde{K}^2e^{-2\widetilde{K}}d\widetilde{K} = \frac{1}{4}, \tag{15a}$$

$$\int_{Fr^{-1}}^{\infty}\widetilde{K}^2e^{-2\widetilde{K}}d\widetilde{K} = \frac{1}{4}(2Fr^{-2}+2Fr^{-1}+1)e^{-2Fr^{-1}} = \frac{1}{4}I_2(Fr), \tag{15b}$$

$$\int_0^{Fr^{-1}}\widetilde{K}^4e^{-2\widetilde{K}}d\widetilde{K} = \frac{1}{4}\left[3-(2Fr^{-4}+4Fr^{-3}+6Fr^{-2}+6Fr^{-1}+3)e^{-2Fr^{-1}}\right] = \frac{1}{4}I_4(Fr). \tag{15c}$$

The I_2 term receives contributions from wavenumbers ranging from $\widetilde{K} = Fr^{-1}$ to $\widetilde{K} = \infty$. The largest contribution of the integrand comes from $\widetilde{K} = 1$ (see the solid line in Fig. 1), which corresponds to the typical horizontal scale of the orography. On the contrary, the I_4 term is made

up of wavenumbers in the range between $\widetilde{K} = 0$ and $\widetilde{K} = Fr^{-1}$, with the largest contribution from the integrand being shifted to a higher wavenumber $\widetilde{K} = 2$ (i.e., half the orography scale; see the dashed line in Fig. 1). The response decays rapidly away from $\widetilde{K} = 1$ for I_2 and $\widetilde{K} = 2$ for I_4, especially towards the high-wavenumber tail of the spectrum (i.e., high-frequency waves). It is noteworthy that this decay depends crucially on the exponential that results directly from the Fourier transform of the terrain elevation, but any smooth topography will have a spectrum that decays towards high wavenumbers (albeit in different ways). Substitution of Eq. (15) into (14) yields

$$\boldsymbol{\tau}_0 = \frac{\Pi}{4}\int_0^{\pi}(\cos\phi, \gamma\sin\phi)\frac{\cos(\phi-\chi)}{\sqrt{\cos^2\phi+\gamma^2\sin^2\phi}}d\phi, \tag{16a}$$

$$\boldsymbol{\tau}_{asy1} = -I_2(Fr)\boldsymbol{\tau}_0, \tag{16b}$$

$$\boldsymbol{\tau}_{asy2} = -\frac{1}{2}Fr^2 I_4(Fr)\left[R_x(\gamma,\chi)\tau_{0x}, R_y(\gamma,\chi)\tau_{0y}\right], \tag{16c}$$

where

$$R_x(\gamma,\chi) = \frac{\int_0^{\pi}\frac{\cos\phi\cos^3(\phi-\chi)}{\sqrt{\cos^2\phi+\gamma^2\sin^2\phi}}d\phi}{\int_0^{\pi}\frac{\cos\phi\cos(\phi-\chi)}{\sqrt{\cos^2\phi+\gamma^2\sin^2\phi}}d\phi}, \tag{17a}$$

$$R_y(\gamma,\chi) = \frac{\int_0^{\pi}\frac{\sin\phi\cos^3(\phi-\chi)}{\sqrt{\cos^2\phi+\gamma^2\sin^2\phi}}d\phi}{\int_0^{\pi}\frac{\sin\phi\cos(\phi-\chi)}{\sqrt{\cos^2\phi+\gamma^2\sin^2\phi}}d\phi}. \tag{17b}$$

$\boldsymbol{\tau}_{asy1}$ is anti-parallel to $\boldsymbol{\tau}_0$, with its magnitude controlled by the I_2 term. $\boldsymbol{\tau}_{asy2}$ is more complicated, depending not only on Fr but also on γ and χ. Given the difference between R_x and R_y, $\boldsymbol{\tau}_{asy2}$ may be misaligned with $\boldsymbol{\tau}_0$. This suggests that NHE can change the direction of the GWMF as well as its magnitude.

In order to better understand the NHE, they are quantified by the ratio between the asymptotic and hydrostatic GWMFs, i.e.,

$$\tilde{\tau}_x(Fr,\gamma,\chi) = \frac{\tau_{asyx}}{\tau_{x0}} = 1 - I_2(Fr) - \frac{1}{2}Fr^2 I_4(Fr) R_x(\gamma,\chi), \tag{18a}$$

$$\tilde{\tau}_y(Fr,\gamma,\chi) = \frac{\tau_{asyy}}{\tau_{y0}} = 1 - I_2(Fr) - \frac{1}{2}Fr^2 I_4(Fr) R_y(\gamma,\chi). \tag{18b}$$

The second term on the right-hand-side (RHS) of Eq. (18) is related to $\boldsymbol{\tau}_{asy1}$ (hereafter, NHE1 for short), which only depends on the horizontal Froude number. It denotes the wave components that are mistaken as vertically-propagating internal waves in the hydrostatic approximation, but are actually evanescent waves. The third term arises from $\boldsymbol{\tau}_{asy2}$ (hereafter, NHE2 for short), which is attributed to the difference between the dispersion relationships of hydrostatic and nonhydrostatic OGWs, i.e., the K^2 term within the brackets of Eq. (1). As noted above, NHE2 can affect both the magnitude and direction of the GWMF.

The above asymptotic expressions were derived for weakly nonhydrostatic OGWs. In the limit $Fr \to 0$, they simplify to

$$\tilde{\tau}_x(Fr \to 0,\gamma,\chi) = 1 - \frac{3}{2}R_x(\gamma,\chi)Fr^2, \tag{19a}$$

$$\tilde{\tau}_y(Fr \to 0,\gamma,\chi) = 1 - \frac{3}{2}R_y(\gamma,\chi)Fr^2. \tag{19b}$$

As will be shown in section 4, the relative difference between the asymptotic and exact GWMFs increases as the horizontal Froude number increases. Therefore, the asymptotic GWMF at $Fr \to \infty$ provides an estimate of the upper bound of the bias. Expanding the $e^{-2Fr^{-1}}$ term in Eq. (18) as $Fr \to \infty$ using Taylor series, one can readily find that

$$\tilde{\tau}_x(Fr \to \infty,\gamma,\chi) = \left[\frac{4}{3} - \frac{2}{5}R_x(\gamma,\chi)\right]Fr^{-3}, \tag{20a}$$

$$\tilde{\tau}_y(Fr \to \infty,\gamma,\chi) = \left[\frac{4}{3} - \frac{2}{5}R_y(\gamma,\chi)\right]Fr^{-3}. \tag{20b}$$

At this highly-nonhydrostatic limit, the GWMF becomes extremely small (proportional to Fr^{-3}), given the trivial contribution from very small-scale OGWs (see Fig. 1). This result is not only qualitatively correct, given that, without adopting the approximation expressed by Eq. (13), the drag would also decrease to zero at high *Fr*, but even approximately quantitatively correct, as will be shown next.

4 Results

In this section, the NHE will be firstly studied for the simple case of a circular mountain, i.e., $\gamma = 1$. Then we will investigate the more general case of elliptical mountains with $\gamma \neq 1$. In the latter case, the mean flow can be either parallel or oblique to the main axes of the mountain, which will be examined separately. These variants will henceforth be called "parallel flow" and "oblique flow", for short.

4.1 Isotropic terrain

For isotropic terrain, without loss of generality, the horizontal wind direction can be set to $\chi = 0$ for simplicity, i.e., $\mathbf{V_0}$ = (U_0, 0). In this case, $\tau_{x0} = \frac{\pi}{4}\bar{\rho}Nh_0^2aU_0$, $\tau_{y0} = 0$, $R_x(1,0) = \frac{3}{4}$, $R_y(1,0) = 0$, and Eq. (18) simplifies to

$$\tilde{\tau}_c(Fr) = 1 - I_2(Fr) - \frac{3}{8}Fr^2 I_4(Fr)$$

$$= 1 - \frac{9}{8}Fr^2 + e^{-2Fr^{-1}}\left(-\frac{5}{4}Fr^{-2} - \frac{1}{2}Fr^{-1} + \frac{5}{4} + \frac{9}{4}Fr + \frac{9}{8}Fr^2\right), \quad (21)$$

where the subscript "*c*" indicates circular terrain. Clearly, $\tilde{\tau}_c$ only depends on the horizonal Froude number.

The variation of $\tilde{\tau}_c$ with the horizontal Froude number is depicted in Fig. 2. For comparison, the scaled asymptotic GWMF in the case of 2D ridge is also shown, which is expressed as follows [cf. Eq. (16) in T08]

$$\tilde{\tau}_{2D}(Fr) = \frac{\tau_{asy\_2D}}{\tau_{0\_2D}} = 1 - \frac{3}{4}Fr^2 + e^{-2Fr^{-1}}\left(-Fr^{-1} + \frac{1}{2} + \frac{3}{2}Fr + \frac{3}{4}Fr^2\right). \quad (22)$$

It is clear that NHE weaken the GWMF. For both 2D and 3D OGWs, the asymptotic GWMFs are in good agreement with their exact counterparts which are obtained via numerical integration of Eq. (11) in this work and Eq. (10) in T08, respectively. The GWMF is only slightly overestimated by Eq. (22) for 2D flow and underestimated by Eq. (12) with respect to Eq. (11) for 3D flow for moderate *Fr*. This justifies the choice of Fr^{-1} as the upper limit of the integral in Eq. (11), given the simplifications this entails. Although adoption of the asymptotic approximation for the GWMF slightly improves the agreement with Eq. (11), the GWMF is still underestimated by a larger fraction than it is overestimated in the 2D case. Note that $\tilde{\tau}_c$ is always smaller than its 2D counterpart. In the limit $Fr \to 0$, $\tilde{\tau}_c(Fr)$ tends asymptotically to $1 - \frac{9}{8}Fr^2$ while $\tilde{\tau}_{2D}$ varies as $1 - \frac{3}{4}Fr^2$. In the opposite limit $Fr \to \infty$, $\tilde{\tau}_c$ and $\tilde{\tau}_{2D}$ tend asymptotically to

$$\tilde{\tau}_c(Fr \to \infty) = \frac{31}{30}Fr^{-3}, \quad (23)$$

$$\tilde{\tau}_{2D}(Fr \to \infty) = \frac{3}{2}Fr^{-2}, \quad (24)$$

respectively. $\tilde{\tau}_c$ is proportional to Fr^{-3} which decays faster than $\tilde{\tau}_{2D}$. As shown by Fig. 2, the way in which $\tilde{\tau}_c$ approaches zero as *Fr* increases is surprisingly accurate (as found in T08 for $\tilde{\tau}_{2D}$) given that the asymptotic approximation was developed for small *Fr*.

As stated in section 3, the NHE can be decomposed into two terms: NHE1 and NHE2. Figure 3 displays these two terms as a function of the horizontal Froude number. The magnitude of NHE1 exhibits an increasing trend with *Fr*. At lower horizontal Froude numbers ($Fr < 0.2$), the NHE1 term is very weak. This is because the lower limit of the integral in Eq. (15b) is given by Fr^{-1}, hence the NHE1 term mainly comes from high-frequency waves which produce negligible GWMF (Fig. 1). As *Fr* increases beyond 0.2 (corresponding to a cutoff horizontal wavenumber of

$\widetilde{K} = 5$), the magnitude of NHE1 term increases rapidly, reaching up to about 0.7 at Fr = 1. As Fr approaches infinity, this term tends asymptotically to -1. The NHE2 term is jointly determined by the squared horizontal Froude number (Fr^2) and I_4 given by Eq. (15c). As the horizontal Froude number increases, each of these two factors increases and decreases, respectively. The latter effect is due to the fact that the upper limit of the integral in Eq. (15c) decreases as Fr increases. As a result, the magnitude of NHE2 firstly increases with Fr, peaking around Fr = 0.48 at a maximum of about 0.1. It then starts decreasing as the horizontal Froude number increases. It is clear that NHE2 plays a more important role in the flow regimes with low Fr whereas NHE1 dominates above about Fr = 0.4.

4.2 Anisotropic terrain: parallel flow

For OGWs generated by elliptical mountains, we firstly study the special case of horizontal wind parallel to the main axes of the orography, which are assumed to be aligned in the x and y directions, i.e., $\chi = 0$ (mean flow along the x axis) or $\chi = \pm\frac{\pi}{2}$ (mean flow along the y axis). In this situation, $\tilde{\boldsymbol{\tau}}$ only depends on the horizontal Froude number and on the terrain anisotropy.

Taking $\chi = 0$ for example, i.e., $\mathbf{V_0} = (U_0, 0)$, one obtains that $\tau_{y0} = 0$, $R_y(\gamma, 0) = 0$, and

$$R_{x0}(\gamma) = R_x(\gamma, 0) = \frac{\int_0^{\pi} \frac{\cos^4\phi}{\sqrt{\cos^2\phi + \gamma^2 \sin^2\phi}} d\phi}{\int_0^{\pi} \frac{\cos^2\phi}{\sqrt{\cos^2\phi + \gamma^2 \sin^2\phi}} d\phi}. \quad (25)$$

Hereafter, the subscript "0" denotes the case with $\chi = 0$. The black line in Fig. 4 shows the variation of $R_{x0}(\gamma)$ with γ. Clearly, $R_{x0}(\gamma)$ increases as γ increases (i.e., from a ridge normal to the flow to a ridge along the flow direction), showing substantial changes (by about 30%) from $\gamma = \frac{1}{10}$ to $\gamma = 10$. The fastest variation occurs near $\gamma = 1$.

To better reveal the influence of terrain anisotropy, the relative variation of $\tilde{\tau}_{x0}(\gamma, Fr)$ with respect to $\tilde{\tau}_c$ is examined, which is defined as

$$\Delta\tilde{\tau}_{x0}(\gamma, Fr) = \frac{\tilde{\tau}_{x0}(\gamma,Fr)-\tilde{\tau}_c(Fr)}{\tilde{\tau}_c(Fr)} = \frac{\tilde{\tau}_{x0}(\gamma,Fr)}{\tilde{\tau}_c(Fr)} - 1. \quad (26)$$

At $Fr = 0$, $\Delta\tilde{\tau}_{x0}$ is always equal to zero (Fig. 5). As the horizontal Froude number increases, the $\Delta\tilde{\tau}_{x0}$ curves quickly diverge. In the case of mean flow perpendicular to the long axis of the mountain ($\gamma < 1$), $\Delta\tilde{\tau}_{x0}$ is greater than zero, i.e., $\tilde{\tau}_{x0}(\gamma, Fr) > \tilde{\tau}_c(Fr)$. This means that the GWMF is less reduced than in the isotropic case, i.e., weakening of NHE. This is consistent with the 2D-3D comparison presented in Fig. 2. In contrast, when the mean flow is aligned with the long axis of the mountain ($\gamma > 1$), NHE are enhanced, as suggested by the negative $\Delta\tilde{\tau}_{x0}$.

The $\Delta\tilde{\tau}_{x0}$ curves become more and more flat as the horizontal Froude number increases, tending asymptotically to their limits at $Fr \to \infty$, i.e.,

$$\Delta\tilde{\tau}_{x0}(\gamma, Fr \to \infty) = \frac{9}{31}\left[1 - \frac{4}{3}R_{x0}(\gamma)\right], \quad (27)$$

which is obtained on substitution of Eqs. (20a) and (23) into Eq. (26). It is clear that the influence of terrain anisotropy is controlled by $R_{x0}(\gamma)$. When the mean flow is aligned with the long axis of the mountain, (the magnitude of) $\Delta\tilde{\tau}_{x0}$ is more notably enhanced than it is suppressed in the case of mean flow perpendicular to the long axis of the mountain. For instance, at $Fr = 1$, $\Delta\tilde{\tau}_{x0}$ exceeds 3% at $\gamma = 8$ while it is less than 3% at $\gamma = \frac{1}{8}$. This difference is attributed to the asymmetric distribution of $R_{x0}(\gamma)$ about $\gamma = 1$ (see the black line in Fig. 4).

While $R_{x0}(\gamma)$ changes substantially with γ, that is not so much the case of $\Delta\tilde{\tau}_{x0}$. For two arbitrary γ, say, (γ_1, γ_2), the difference between their $\Delta\tilde{\tau}_{x0}$ gradually saturates as $Fr \to \infty$, i.e.,

$$\Delta\tilde{\tau}_{x0}(\gamma_1, Fr \to \infty) - \Delta\tilde{\tau}_{x0}(\gamma_2, Fr \to \infty) = \frac{12}{31}[R_{x0}(\gamma_2) - R_{x0}(\gamma_1)]. \quad (28)$$

This means that the influence of terrain anisotropy on $R_{x0}(\gamma)$ can be only partially projected onto $\Delta\tilde{\tau}_{x0}$, since the latter is at most $\frac{12}{31} \approx 40\%$ of the former. From Eq. (25), $R_{x0}(\gamma)$ equals $\frac{2}{3}$ and 1 at $\gamma = 0$ and $\gamma \to \infty$, respectively. Bounded by the lower and upper limits of $R_{x0}(\gamma)$, the variation of $\Delta\tilde{\tau}_{x0}$ with γ is thus always smaller than $\frac{12}{31} \times \left(1 - \frac{2}{3}\right) = \frac{4}{31} \approx 12.9\%$. When compared to NHE in the isotropic orography case, i.e., $R_{x0}(1) = \frac{3}{4}$, the maximum positive and negative differences are $\frac{12}{31} \times \left(1 - \frac{3}{4}\right) = \frac{3}{31} \approx 9.7\%$ and $\frac{12}{31} \times \left(\frac{2}{3} - \frac{3}{4}\right) = -\frac{1}{31} \approx -3.2\%$, respectively.

From the above analysis, we can see that NHE in the parallel-flow case are only weakly affected by terrain anisotropy. Instead, it is the horizontal Froude number that greatly impacts $\tilde{\tau}_{x0}$, and this occurs both in the cases of circular mountains and 2D ridges (see section 4.1). Physically, when the mean flow is parallel to the main axis of the elliptical terrain, e.g., when $\chi = 0$, as studied, the horizontal Froude number is simplified to $Fr = \frac{|\tilde{\mathbf{V}}_0|}{Na} = \frac{U_0}{Na}$. Thus, the terrain width in the cross-flow direction has little contribution to the flow advection time.

4.3 Anisotropic terrain: oblique flow

In this section, the general case of mean flow oblique to the main axes of the elliptical bell-shaped mountain is examined to understand more thoroughly the impacts of terrain anisotropy and horizontal wind direction on the asymptotic GWMF expression.

In addition to $\chi = 0$, Figure 4 also shows the variation of $R_x(\gamma, \chi)$ as a function of γ for three different horizontal wind directions, i.e., $\chi = \frac{\pi}{8}$, $\frac{\pi}{4}$ and $\frac{3\pi}{8}$. These wind directions are chosen in the range of $\left[0, \frac{\pi}{2}\right)$, but the same results can be obtained for χ in the range of $\left[0, -\frac{\pi}{2}\right)$. This is because $R_x(\gamma, \chi)$ is symmetric about $\chi = 0$, i.e., $R_x(\gamma, \chi) = R_x(\gamma, -\chi)$ in accordance with Eq. (17a). (Note that $R_x(\gamma, \chi)$ is ill-defined at $\chi = \pm\frac{\pi}{2}$ where τ_{x0} vanishes.) The variation of $R_y(\gamma, \chi)$

393 is not presented herein, but can be inferred from that of $R_x(\gamma,\chi)$ because $R_x(\gamma,\chi) =$
394 $R_y\left(\frac{1}{\gamma},\frac{\pi}{2}-\chi\right)$. In the situation with $\chi=\frac{\pi}{8}$, $R_x(\gamma,\chi)$ increases as γ increases, which is similar to
395 the case with $\chi=0$. When χ equals $\frac{\pi}{4}$ or $\frac{3\pi}{8}$, $R_x(\gamma,\chi)$ instead decreases as γ increases. This
396 suggests a change in the trend of $R_x(\gamma,\chi)$ with γ for a horizontal wind direction between $\chi=\frac{\pi}{8}$
397 and $\chi=\frac{\pi}{4}$, at which $R_x(\gamma,\chi)$ should be independent of γ. As can be seen below, this occurs at
398 $\chi=\frac{\pi}{6}$.

399 The distribution of $R_x(\gamma,\chi)$ in γ-χ parameter space is shown in Fig. 6, with γ and χ in the
400 ranges of $\left[\frac{1}{10},10\right]$ and $\left[0,\frac{\pi}{2}\right)$, respectively. $R_x(\gamma,\chi)$ is always equal to $\frac{3}{4}$ at $\chi=\frac{\pi}{6}$, which can be
401 obtained analytically from Eq. (17a). Remember that $R_x(\gamma,\chi)\equiv\frac{3}{4}$ at $\gamma=1$ as well (see section
402 4.1). Therefore, the γ-χ space can be divided into four quadrants by the lines $\chi=\frac{\pi}{6}$ and $\gamma=1$. In
403 the third and fourth quadrants ($0\le\chi<\frac{\pi}{6}$), $R_x(\gamma,\chi)$ has an increasing trend with γ. The more the
404 horizontal wind is aligned with the long axis of the elliptical mountain, the more markedly terrain
405 anisotropy affects $R_x(\gamma,\chi)$. The greatest variation of $R_x(\gamma,\chi)$ with γ $\left(R_{x0}(\gamma\to\infty)-R_{x0}(\gamma\to\right.$
406 $\left.0)\right)$ occurs at $\chi=0$, which takes the value $\frac{1}{3}$, as derived in section 4.2. In the first and second
407 quadrants (i.e., $\frac{\pi}{6}<\chi<\frac{\pi}{2}$), $R_x(\gamma,\chi)$ decreases instead as γ increases, and the influence of terrain
408 anisotropy becomes larger with χ. In the limit of $\chi=\frac{\pi}{2}$, $R_x\left(\gamma,\frac{\pi}{2}\right)$ is ill-defined, yet it is equivalent
409 to $R_y\left(\frac{1}{\gamma},0\right)$ which is well defined. From Eq. (17b), $R_x\left(\gamma\to0,\frac{\pi}{2}\right)=R_y(\gamma\to\infty,0)=1$, and
410 $R_x\left(\gamma\to\infty,\frac{\pi}{2}\right)=R_y(\gamma\to0,0)=\frac{1}{3}$. As a result, the greatest variation of $R_x(\gamma,\chi)$ with γ is $\frac{2}{3}$, i.e.
411 twice that for $\chi=0$. Similarly, the greatest variations of $R_x(\gamma,\chi)$ with χ (i.e., variations along the

412 vertical rather than horizontal direction in the graph) on the left- and right semi-planes of the γ-χ
413 parameter space are $\frac{1}{3}$ and $\frac{2}{3}$, respectively.

414 As in the parallel-flow case, the relative variation of $\tilde{\tau}_x(\gamma, Fr)$ with respect to $\tilde{\tau}_c$ is also
415 examined here, which is defined as

416 $$\Delta\tilde{\tau}_x(\gamma, \chi, Fr) = \frac{\tilde{\tau}_x(\gamma,\chi,Fr)-\tilde{\tau}_c(Fr)}{\tilde{\tau}_c(Fr)} = \frac{\tilde{\tau}_x(\gamma,\chi,Fr)}{\tilde{\tau}_c(Fr)} - 1. \quad (29)$$

417 As $Fr \to \infty$, $\tilde{\tau}_x$ tends asymptotically to

418 $$\tilde{\tau}_x(\gamma, \chi, Fr \to \infty) = \frac{9}{31}\left[1 - \frac{4}{3}R_x(\gamma, x)\right]. \quad (30)$$

419 For two pairs of (γ, χ), e.g., (γ_1, χ_1) and (γ_2, χ_2), the difference between their $\tilde{\tau}_x$ is

420 $$\tilde{\tau}_x(\gamma_1, \chi_1, Fr \to \infty) - \tilde{\tau}_x(\gamma_2, \chi_2, Fr \to \infty) = \frac{12}{31}[R_x(\gamma_2, \chi_2) - R_x(\gamma_1, \chi_1)]. \quad (31)$$

421 Again, this means that the influences of terrain anisotropy and horizontal wind direction on
422 $R_x(\gamma, \chi)$ have a relatively small impact on $\tilde{\tau}_x$. From Fig. 6, the global maximal variation of
423 $R_x(\gamma, \chi)$ with γ and χ is $\frac{2}{3}$. Thus, under the influence of both terrain anisotropy and horizontal
424 wind direction, $\tilde{\tau}_x$ can change by $\frac{12}{31} \times \frac{2}{3} \approx 25.8\%$ at most as *Fr* tends to infinity. Compared to the
425 NHE in the isotropic terrain case, the maximum positive and negative differences are
426 $\frac{12}{31} \times \left(1 - \frac{3}{4}\right) = \frac{3}{31} \approx 9.7\%$ and $\frac{12}{31} \times \left(\frac{1}{3} - \frac{3}{4}\right) = -\frac{5}{31} \approx -16.1\%$, respectively. At small horizontal
427 Froude number, the impacts of terrain anisotropy and horizontal wind direction are rather weak,
428 as will be shown below.

429 Figure 7 gives the distributions of $\Delta\tilde{\tau}_x$ on the γ-χ plane at four different horizontal Froude
430 numbers: *Fr* = 0.1, 0.3, 0.5, and 1.0, respectively. Positive $\Delta\tilde{\tau}_x$ is found in the first and third
431 quadrants, indicating an amplification of the NHE compared to the case of isotropic orography.
432 Conversely, NHE are weakened in the second and fourth quadrants, given the negative values of

433 $\Delta\tilde{\tau}_x$ existing there. At *Fr* = 0.1 (Fig. 7a) $\Delta\tilde{\tau}_x$ is extremely small, implying that the terrain
434 anisotropy and horizontal wind direction have negligible influence on the NHE. At *Fr* = 0.3 (Fig.
435 7b), the impacts of terrain anisotropy and horizontal wind direction increase by more than 10 times
436 compared to those at *Fr* = 0.1. When the horizontal Froude number further increases to *Fr* = 0.5
437 and 1.0 (Figs. 7c, 7d), there occurs a consistent increase in the magnitude of $\Delta\tilde{\tau}_x$, which can reach
438 up to 0.1 in the first quadrant (i.e., $\gamma > 1$ and $\frac{\pi}{6} < \chi < \frac{\pi}{2}$).

439 Figure 8 displays the variation of $\tilde{\tau}_x$ as a function of *Fr*. Two elliptical mountains with $\gamma =$
440 $\frac{1}{8}$ (dashed lines) and $\gamma = 8$ (solid lines) are selected, along with two horizontal wind directions
441 $\chi = \frac{\pi}{8}$ (blue lines) and $\chi = \frac{3\pi}{8}$ (red lines). From the above analysis, these configurations of terrain
442 anisotropy and horizontal wind direction tend to have a significant influence on the NHE. However,
443 as can be seen from Fig. 8, $\tilde{\tau}_x$ is still mainly determined by *Fr*. At *Fr* = 0.1, $\tilde{\tau}_x = 0.99$, i.e., the
444 OGWs are almost purely hydrostatic. As *Fr* increases, $\tilde{\tau}_x$ decreases rapidly to about 0.65 at *Fr* =
445 0.5, and further reduces to about 0.27 at *Fr* = 1.0. Compared with the horizontal Froude number,
446 terrain anisotropy and horizontal wind direction only play a minor role. This is due to the fact that
447 these two factors only affect the NHE2 term [see Eq. (18)]. At small horizontal Froude number
448 (*Fr* < 0.2), the NHE2 term is of greater importance than NHE1 (Fig. 2), but $\Delta\tilde{\tau}_x$ is too weak to
449 exert a profound influence on $\tilde{\tau}_x$ (Fig. 7a). At moderate to large horizontal Froude number (*Fr* >
450 0.4), while $\Delta\tilde{\tau}_x$ is significantly enhanced (Figs. 7c, 7d), the NHE2 term is exceeded by NHE1, thus
451 contributing less to $\tilde{\tau}_x$.

452 4.4 Surface pressure perturbation

453 Theoretically, the GWMF is equal to the pressure drag at the surface (e.g., Teixeira et al.
454 2004). In this section, the surface pressure perturbations are investigated to help understand the
455 impact of NHE on the GWMF. Herein, we only focus on the simple case of mean flow over circular

456 bell-shaped mountains, because the horizontal wind direction and orography anisotropy play a
457 minor role on the NHE (as we have just seen).

458 Figure 9 depicts the distribution of the surface pressure perturbation obtained via numerical
459 integration of Eqs. (A4). Note that the pressure perturbations are scaled with $\bar{\rho}N\left|\widetilde{\mathbf{V}}\right|h_0$. At Fr =
460 0.1, the pressure field (Fig. 9a) shows a left-right anti-symmetric pattern about the orography
461 center, with positive and negative regions on the windward and leeward slope respectively (Smith
462 1980; Teixeira et al. 2004). In this weakly nonhydrostatic case, the pressure perturbation mainly
463 arises from vertically-propagating OGWs, with little contribution from evanescent waves (Figs.
464 9b, 9c). At Fr = 0.5, however, the surface pressure perturbation ceases to be perfectly anti-
465 symmetric about the mountain center (Fig. 9d). The maximum on the windward slope weakens
466 slightly as compared to that at Fr = 0.1, while the minimum on the lee slope also weakens notably
467 and moves downstream. In addition, a secondary pressure minimum occurs near the orography
468 center. This more complex pressure pattern is due to an enhanced pressure contribution from
469 evanescent waves (Fig. 9f), which is symmetric about the orography center (and thus produces
470 zero surface pressure drag). Concurrently, the pressure perturbation associated with vertically-
471 propagating OGWs weakens (Fig. 9e), giving rise to the reduction of GWMF.

472 Using the Taylor series expansion of the vertical wavenumber at small Fr (expressed by
473 Eq. (13)), one can also derive an asymptotic expression for the pressure perturbation associated
474 with vertically-propagating OGWs (see details in Appendix A), which is decomposed into three
475 parts (namely, p_0, p_1 and p_2) corresponding to $\boldsymbol{\tau}_0$, $\boldsymbol{\tau}_{asy1}$ and $\boldsymbol{\tau}_{asy2}$, respectively.

476 Figure 10 shows the distribution of the asymptotic surface pressure perturbation at Fr =
477 0.1, which is also scaled by $\bar{\rho}N\left|\widetilde{\mathbf{V}}\right|h_0$. The total asymptotic pressure perturbation (Fig. 10a) agrees
478 well with that in Fig. 9a. It is dominated by the hydrostatic part (Fig. 10b), because NHE are very

weak at Fr = 0.1 (see Fig. 2). The maximum (minimum) pressure perturbation occurs about one half-width away from the orography center, suggesting that the horizontal scale of the dominant wave field is comparable to that of the mountain. This is consistent with the power spectrum of $\boldsymbol{\tau}_0$, which peaks at $\widetilde{K} = 1$, i.e., $K = a^{-1}$ (Fig. 1). The p_1 pressure perturbation is extremely small (Fig. 10c), given the small magnitude of $\boldsymbol{\tau}_{asy1}$ at this low horizontal Froude number (Fig. 3). A wave-train pattern is found both upstream and downstream of the mountain, which can be ascribed to the $\cos\left(\frac{\mu}{Fr}\right)$ and $\sin\left(\frac{\mu}{Fr}\right)$ terms in Eq. (A9b). This pattern is undiscernible in Fig. 10a because of its small magnitude. The horizontal wavelength of p_1 is very short, since it originates mainly from the high-frequency part of the wave spectrum [Eq. (A7b)]. Similar to p_0, the p_2 pressure perturbation is anti-symmetric about the orography center (Fig. 10d), but with negative (positive) perturbations on the upslope (downslope) side. Consequently, p_2 produces a pressure gradient force opposed to that of p_0, contributing negatively to the total surface pressure drag. Moreover, the p_2 pressure perturbation is mainly confined to the region within one half-width of the mountain to the orography center. This is also in agreement with the power spectrum of $\boldsymbol{\tau}_{asy2}$ which peaks at $\widetilde{K} = 2$ (Fig. 1).

Figure 11 is similar to Fig. 10, but for Fr = 0.5. Compared to that at Fr = 0.1, the total pressure perturbation is substantially reduced (Fig. 11a). The pressure perturbation extrema only correspond to about 70% of those at Fr = 0.1. The scaled p_0 (Fig. 11b) is independent of Fr, so it is exactly the same as in Fig. 10b. The p_1 pressure perturbation (Fig. 11c) increases markedly in magnitude, reaching up to 60% of p_0. The p_2 pressure perturbation is also enhanced (Fig. 11d). However, unlike in the case with Fr = 0.1, p_2 is smaller than p_1. This agrees with the major role played by the NHE1 term at moderate-to-large horizontal Froude numbers (see Fig. 3). Moreover, while the p_1 and p_2 pressure perturbations still display a wave-train pattern upstream and

downstream of the mountain, their horizontal wavelengths have increased significantly. Taking p_1 as an example, the dominant wavelength is approximately twice the orography half-width. This is because, at Fr = 0.5, p_1 is composed of wavenumbers ranging from $\widetilde{K} = 2$ to ∞ [see Eq. (A7b)]. In this spectral range, the greatest response of $\boldsymbol{\tau}_{asy1}$ corresponding to p_1 occurs at $\widetilde{K} = 2$ (Fig. 1). Owing to the enhanced p_1 pressure perturbation, the extrema of the total pressure perturbation slightly move away from the orography center (Fig. 11a), implying an increase in the dominant wavelength. This is reasonable, since short waves are removed by the NHE from the range of waves that contribute to the GWMF.

5 Summary and discussion

It has been widely recognized that the parameterization of subgrid-scale orographic gravity waves (OGWs) is essential for accurate numerical weather forecast and climate prediction. Many efforts have been made to improve the representation of orographic gravity wave momentum flux (GWMF) and its deposition into the mean flow in numerical models. With the development of high-resolution global numerical weather prediction (NWP) and general circulation models (GCMs), the horizontal scale of unresolved OGWs is becoming increasingly small. As a result, the GWMF can be significantly impacted by nonhydrostatic effects (NHE). However, these effects are not accounted for in even the state-of-the-art parameterization schemes, since there is in general no analytical solution for nonhydrostatic OGWs. In some parametrizations (e.g., Lott and Miller 1997), the GWMF reduction that is known to occur for highly non-hydrostatic waves is mimicked rather artificially by filtering the orography that is fed into the OGW parametrization. The present study proposes the more physical approach of explicitly evaluating the NHE approximately.

Using linear gravity wave theory, we have derived an asymptotic solution for the surface GWMF of 3D OGWs, which is an extension of the 2D asymptotic expression studied in T08. The intensity of the NHE can be quantified by the non-dimensional parameter called here the horizonal Froude number, i.e., $Fr = \frac{|\tilde{\mathbf{V}}_0|}{Na}$. This parameter is akin to the inverse non-dimensional mountain half width $\frac{Na}{U}$ used in previous studies (e.g., Durran and Klemp 1983; Xue and Thorpe 1991; Zängl 2003) but with U replaced by $\widetilde{\mathbf{V}}_0 = (U_0, \gamma V_0)$. This extended definition is necessary due to the horizontal anisotropy of the isolated orography that generates the 3D OGWs.

Based upon an asymptotic approach, the NHE are divided into two components (NHE1 and NHE2). The first component accounts for the high-frequency parts of the wave spectrum (i.e., short waves) that are mistaken as hydrostatic, upward-propagating waves in the hydrostatic approximation. The GWMF associated with NHE1 is parallel but opposite to the hydrostatic GWMF. The second component is due to the difference between the dispersion relationships of hydrostatic and nonhydrostatic OGWs. While NHE1 only depends on the horizontal Froude number, NHE2 also depends on the terrain anisotropy and horizontal wind direction. In the presence of NHE, both the magnitude and direction of GWMF can be changed.

The asymptotic GWMF expression derived here was investigated for OGWs forced by both circular and elliptical mountains for flows with various orientations. In the isotropic orography case, NHE only depend on the horizontal Froude number, which is the same dependence as in the 2D-ridge case studied by T08. Compared to its 2D counterpart, the 3D GWMF is more strongly reduced by NHE. Considering the two parts of the NHE, NHE1 is weaker than NHE2 at lower horizontal Froude number, but its magnitude grows rapidly as the horizontal Froude number increases. On the contrary, NHE2 firstly increases but then starts decreasing with the horizontal

Froude number, with this change of trend occurring at about Fr = 0.48. Consequently, NHE1 starts to be dominant in the reduction of the GWMF above about Fr = 0.4.

For OGWs generated by anisotropic terrain, when the mean flow is perpendicular to the long axis of the orography ($\gamma < 1$), the GWMF is less reduced than in the isotropic case, suggesting a weakening of the NHE. This is consistent with the results of OGWs forced by 2D ridges. Conversely, NHE are enhanced when the mean flow is parallel to the long axis or the orography ($\gamma > 1$). In the parallel-flow case, the NHE vary by no more than 12.9% with the terrain anisotropy, and this occurs as the horizontal Froude number tends asymptotically to infinity. Since this corresponds to a situation in which $\boldsymbol{\tau}$ approaches zero, the relevance of this effect is even more limited. When the mean flow is oblique to the main axes of the mountain, NHE exhibit a greater variation under the joint influence of terrain anisotropy and horizontal wind direction, with a maximum value twice that of the parallel-flow case. Nevertheless, in either case, it is still the horizontal Froude number that dominates the variation of the NHE.

Given the relatively weak influence of terrain anisotropy and horizontal wind direction on the NHE, the asymptotic solution of the GWMF for isotropic terrain [i.e., Eq. (21)], which is simply a function of the horizontal Froude number, may be used to quantify the NHE with a good accuracy. Benefiting from the analytical form of this expression, the parameterization schemes for hydrostatic OGWs can be easily extended to nonhydrostatic conditions, which will inevitably occur in high-resolution NWP and GCMs. It is noteworthy that the horizontal Froude number depends on the horizontal scale of subgrid-scale orography, which is constrained by the model's horizontal resolution. Since the NHE are scale-aware (or scale-dependent), they make the parametrization itself scale-aware. Recently, variable-resolution numerical models have generated a growing interest (e.g., Skamarock et al. 2012; Davis et al. 2016; Zhou et al. 2019; Zhang et al.

2019), as they can significantly reduce the computational costs, while allowing for high-resolution modelling in areas of specific interest. A nonhydrostatic parameterization scheme will be particularly useful for models with variable-resolution meshes, as it can adjust the parameterized GWMF in the fine-resolution regions where NHE are expected to be important, while having little influence in the coarse-resolution areas.

In our upcoming research, a traditional hydrostatic OGW parameterization scheme will be revised taking into account NHE, based on the asymptotic expressions derived in the present study. Then the revised scheme will be implemented in a high-resolution numerical model (with a grid spacing on the order of 10 km) to investigate the impacts of NHE on the vertical momentum transport of subgrid-scale OGWs and their consequences for the large-scale circulation.

Acknowledgements. This work is jointly supported by the National Science Foundation of China (Grants 41875068, 91837207), the Second Tibetan Plateau Scientific Expedition and Research (STEP) program (Grant 2019QZKK0105), and the Beijing Climate Center (QHMS2020002).

Appendix A: Derivation of the asymptotic pressure perturbation at the surface

According to Eq. (7) in Xu et al. (2017b), for 3D OGWs generated by constant flow over an isolated mountain, the polarization relation between the pressure and vertical velocity perturbations in spectral space has the simple form:

$$\hat{p}(k,l,z) = -i\frac{\bar{\rho}}{K^2}\widehat{D}\frac{\partial \hat{w}(z)}{\partial z}. \tag{A1}$$

Substitution of Eq. (3) into the above equation yields

$$\hat{p}(k,l,z) = i\bar{\rho}\frac{\widehat{D}^2}{K^2}me^{imz}\hat{h}(k,l). \tag{A2}$$

Using inverse 2D Fourier transforms, the pressure perturbation in physical space is given by

$$p(x,y,z) = Re\left[i\bar{\rho}\int_{-\infty}^{\infty}\int_{-\infty}^{\infty}\frac{\hat{D}^2}{K^2}m\hat{h}(k,l)\,e^{i(kx+ly+mz)}dkdl\right], \quad \text{(A3)}$$

where $Re(\cdot)$ denotes the real part of a complex number. For the elliptical bell-shaped mountain under consideration, and using polar coordinates for the horizontal wavenumber [see Eq. (8)], the pressure perturbation of nonhydrostatic OGWs at $z = 0$ is

$$p(x,y,0) = p(S,\Psi,0) = Re\left[\frac{i}{\pi}\bar{\rho}N\left|\widetilde{\mathbf{V}}\right|h_0\int_0^{\pi}\int_0^{\infty}\frac{\cos(\phi-\chi)}{\sqrt{\cos^2\phi+\gamma^2\sin^2\phi}}\times\right.$$

$$\left.\sqrt{1-\left[\widetilde{K}Fr\cos(\phi-\chi)\right]^2}\widetilde{K}e^{-\widetilde{K}}e^{i\widetilde{K}S\cos(\phi-\Psi)}d\widetilde{K}d\phi\right], \quad \text{(A4a)}$$

which can be divided into two parts, i.e.,

$$p_{GW}(S,\Psi,0) = Re\left[\frac{i}{\pi}\bar{\rho}N\left|\widetilde{\mathbf{V}}\right|h_0\int_0^{\pi}\int_0^{[Fr\,\cos(\phi-\chi)]^{-1}}\frac{\cos(\phi-\chi)}{\sqrt{\cos^2\phi+\gamma^2\sin^2\phi}}\times\right.$$

$$\left.\sqrt{1-\left[\widetilde{K}Fr\cos(\phi-\chi)\right]^2}\widetilde{K}e^{-\widetilde{K}}e^{i\widetilde{K}S\cos(\phi-\Psi)}d\widetilde{K}d\phi\right]. \quad \text{(A4b)}$$

$$p_{evascent}(S,\Psi,0) = Re\left[\frac{i}{\pi}\bar{\rho}N\left|\widetilde{\mathbf{V}}\right|h_0\int_0^{\pi}\int_{[Fr\,\cos(\phi-\chi)]^{-1}}^{\infty}\frac{\cos(\phi-\chi)}{\sqrt{\cos^2\phi+\gamma^2\sin^2\phi}}\times\right.$$

$$\left.\sqrt{1-\left[\widetilde{K}Fr\cos(\phi-\chi)\right]^2}\widetilde{K}e^{-\widetilde{K}}e^{i\widetilde{K}S\cos(\phi-\Psi)}d\widetilde{K}d\phi\right]. \quad \text{(A4c)}$$

for vertically-propagating OGWs and evanescent waves, respectively. In the deduction of the above equations, the following elliptical polar coordinate in physical space was introduced for convenience:

$$X = \frac{x}{a} = S\cos\Psi,\ Y = \frac{y}{b} = S\sin\Psi, \quad \text{(A5)}$$

where $S = \frac{1}{a}\sqrt{x^2+(\gamma y)^2}$ and $\Psi = \operatorname{atan}\left(\frac{\gamma y}{x}\right)$.

By expanding the vertical wavenumber for small Fr [see Eq. (13)], the asymptotic surface pressure perturbation associated with vertically propagating OGWs can be approximated by the sum of p_0, p_1 and p_2, namely,

$$p_0(S,\Psi,0) = Re\left[\frac{i}{\pi}\bar{\rho}N\left|\widetilde{\mathbf{V}}\right|h_0\int_0^{\pi}\frac{\cos(\phi-\chi)}{\sqrt{\cos^2\phi+\gamma^2\sin^2\phi}}G_0(\varphi,S,\Psi)d\phi\right], \tag{A6a}$$

$$p_1(S,\Psi,0) = Re\left[-\frac{i}{\pi}\bar{\rho}N\left|\widetilde{\mathbf{V}}\right|h_0\int_0^{\pi}\frac{\cos(\phi-\chi)}{\sqrt{\cos^2\phi+\gamma^2\sin^2\phi}}G_1(\varphi,S,\Psi)d\phi\right], \tag{A6b}$$

$$p_2(S,\Psi,0) = Re\left[-\frac{i}{2\pi}Fr^2\bar{\rho}N\left|\widetilde{\mathbf{V}}\right|h_0\int_0^{\pi}\frac{\cos^3(\phi-\chi)}{\sqrt{\cos^2\phi+\gamma^2\sin^2\phi}}G_2(\varphi,S,\Psi)d\phi\right], \tag{A6c}$$

with G_0, G_1 and G_2 given, respectively, by

$$G_0(\phi,S,\Psi) = \int_0^{\infty}\widetilde{K}\,e^{\widetilde{K}[iS\cos(\phi-\Psi)-1]}d\widetilde{K} = Q^{-2}, \tag{A7a}$$

$$G_1(\phi,S,\Psi) = \int_{Fr^{-1}}^{\infty}\widetilde{K}\,e^{\widetilde{K}[iS\cos(\phi-\Psi)-1]}d\widetilde{K} = Q^{-2}e^{-QFr^{-1}}(1+QFr^{-1}), \tag{A7b}$$

$$\begin{aligned} G_2(\phi,S,\Psi) &= \int_0^{Fr^{-1}}\widetilde{K}^3\,e^{\widetilde{K}[iS\cos(\phi-\Psi)-1]}d\widetilde{K} \\ &= Q^{-4}\left[6-e^{-QFr^{-1}}(Q^3Fr^{-3}+3Q^2Fr^{-2}+6QFr^{-1}+6)\right], \end{aligned} \tag{A7c}$$

and

$$Q(\phi,S,\Psi) = 1-iS\cos(\phi-\Psi) = 1-i\mu(\phi,S,\Psi). \tag{A8}$$

Clearly, p_0 is the pressure perturbation of purely hydrostatic OGWs while p_1 and p_2 are the pressure perturbations corresponding to $\boldsymbol{\tau}_{asy1}$ and $\boldsymbol{\tau}_{asy2}$.

Finally, after some lengthy but straightforward algebraic manipulations, one can obtain the three components of the surface pressure perturbation associated with vertically-propagating OGWs:

$$p_0(S,\Psi,0) = -\frac{\bar{\rho}N|\widetilde{\mathbf{V}}|h_0}{\pi}\int_0^{\pi}\frac{\cos(\phi-\chi)}{\sqrt{\cos^2\phi+\gamma^2\sin^2\phi}}\frac{2\mu}{(1+\mu^2)^2}d\phi, \tag{A9a}$$

$$p_1(S,\Psi,0) = \frac{\bar{\rho}N|\widetilde{\mathbf{V}}|h_0}{\pi}\int_0^{\pi}\frac{\cos(\phi-\chi)}{\sqrt{\cos^2\phi+\gamma^2\sin^2\phi}}\frac{1}{(1+\mu^2)^2}\frac{J_1(\mu)\cos\left(\frac{\mu}{Fr}\right)+J_2(\mu)\sin\left(\frac{\mu}{Fr}\right)}{e^{Fr^{-1}}}d\phi, \tag{A9b}$$

$$p_2(S,\Psi,0)=\frac{\bar{\rho}N|\tilde{\mathbf{V}}|h_0}{2\pi}\int_0^{\pi}\frac{\cos^3(\phi-\chi)}{\sqrt{\cos^2\phi+\gamma^2\sin^2\phi}}\frac{Fr^2}{(1+\mu^2)^4}\left[J_0(\mu)-\frac{J_3(\mu)\cos\left(\frac{\mu}{Fr}\right)+J_4(\mu)\sin\left(\frac{\mu}{Fr}\right)}{e^{Fr^{-1}}}\right]d\phi, \quad \text{(A9c)}$$

where

$$J_0(\mu)=24(1-\mu^2)\mu, \quad \text{(A10a)}$$

$$J_1(\mu)=\mu\left(2+\frac{1+\mu^2}{Fr}\right), \quad \text{(A10b)}$$

$$J_2(\mu)=1-\mu^2+\frac{1+\mu^2}{Fr}, \quad \text{(A10c)}$$

$$J_3(\mu)=\mu\left[24(1-\mu^2)-\frac{6(\mu^2-3)(1+\mu^2)}{Fr}+\frac{6(1+\mu^2)^2}{Fr^2}+\frac{(1+\mu^2)^3}{Fr^3}\right], \quad \text{(A10d)}$$

$$J_4(\mu)=6(\mu^4-6\mu^2+1)+\frac{6(1+3\mu^2)(1-\mu^2)}{Fr}+\frac{3(1-\mu^2)(1+\mu^2)^2}{Fr^2}+\frac{(1+\mu^2)^3}{Fr^3}. \quad \text{(A10e)}$$

References

Amemiya, A., and K. Sato, 2016: A new gravity wave parameterization including three-dimensional propagation. *J. Meteor. Soc. Japan*, **94**, 237–256, https://doi.org/10.2151/jmsj.2016-013

Beljaars, A. C. M., A. R. Brown, and N. Wood, 2004: A new parametrization of turbulent orographic form drag. *Quart. J. Roy. Meteor. Soc.*, **130**, 1327–1347, https://doi.org/10.1256/qj.03.73

Broutman, D., J. W. Rottman, and S. D. Eckermann, 2002: Maslov's method for stationary hydrostatic mountain waves. *Quart. J. Roy. Meteor. Soc.*, **128,** 1159–1171, https://doi.org/10.1256/003590002320373247

Broutman, D., J. W. Rottman, and S. D. Eckermann, 2003: A simplified Fourier method for nonhydrostatic mountain waves. *J. Atmos. Sci.*, **60**, 2686–2696, https://doi.org/10.1175/1520-0469(2003)060%3C2686:ASFMFN%3E2.0.CO;2

Davis, C. A., D. A. Ahijevych, W. Wang, and W. C. Skamarock, 2016: Evaluating medium-range tropical cyclone forecasts in uniform- and variable-resolution global models. Mon. Wea. Rev., **144**, 4141–4160, https://doi.org/10.1175/MWR-D-16-0021.1

Doyle, J. D., and D. R. Durran, 2002: The dynamics of mountain-wave-induced rotors. *J. Atmos. Sci.*, **59**, 186–201, https://doi.org/10.1175/1520-0469(2002)059%3C0186:TDOMWI%3E2.0.CO;2

Eckermann, S. D., J. Ma, and D. Broutman, 2015: Effects of horizontal geometrical spreading on the parameterization of orographic gravity wave drag. Part I: Numerical transform solutions. *J. Atmos. Sci.*, **72**, 2330–2347, https://doi.org/10.1175/ JAS-D-14-0147.1

Ehard, B., and Coauthors, 2017: Vertical propagation of large-amplitude mountain waves in the vicinity of the polar night jet. *J. Geophys. Res. Atmos.*, **122**, 1423–1436, https://doi.org/10.1002/2016JD025621

Fritts, D. C., and M. J. Alexander, 2003: Gravity wave dynamics and effects in the middle atmosphere. *Rev. Geophys.*, **41**, 1003, https://doi.org/10.1029/2001RG000106

Grubišić, V., and P. K. Smolarkiewicz, 1997: The effect of critical levels on 3D orographic flows: Linear regime. *J. Atmos. Sci.*, **54**, 1943–1960. https://doi.org/10.1175/1520-0469(1997)054<1943:TEOCLO>2.0.CO;2

Guarino, M.-V., and M. A. C. Teixeira, 2017: Non-hydrostatic effects on mountain wave breaking in directional shear flows. *Quart. J. Roy. Meteor. Soc.*, **143**, 3291–3297. https://doi.org/10.1002/qj.3157

Kim, Y.-J., and A. Arakawa, 1995: Improvement of orographic gravity wave parameterization using a mesoscale gravity wave model. *J. Atmos. Sci.*, **52**, 1875–1902, https://doi.org/10.1175/1520-0469(1995)052%3C1875:IOOGWP%3E2.0.CO;2

Kim, Y. -J., and J. D. Doyle, 2005: Extension of an orographic-drag parameterization scheme to incorporate orographic anisotropy and flow blocking. *Quart. J. Roy. Meteor. Soc.*, **131**, 1893–1921, https://doi.org/10.1256/qj.04.160

Kim, Y. -J., S. D. Eckermann, and H. Y. Chun, 2003: An overview of the past, present and future of gravity-wave drag parametrization for numerical climate and weather prediction models. *Atmos.– Ocean*, **41**, 65–98, https://doi.org/10.3137/ao.410105

679 Klemp, J. B., and D. R. Durran, 1983: An upper boundary condition permitting internal gravity
680 wave radiation in numerical mesoscale models. *Mon. Wea. Rev.*, **111**, 430–444,
681 https://doi.org/10.1175/1520-0493(1983)111%3C0430:AUBCPI%3E2.0.CO;2

682 Lott, F., and M. Miller, 1997: A new sub-grid orographic drag parameterization: Its formulation
683 and testing. *Quart. J. Roy. Meteor. Soc.*, **123**, 101–127,
684 https://doi.org/10.1002/qj.49712353704.

685 Marks, C. J., and S. D. Eckermann, 1995: A three-dimensional nonhydrostatic ray-tracing model
686 for gravity waves: Formulation and preliminary results for the Middle atmosphere. *J.*
687 *Atmos. Sci.*, **52**, 1959–1984, https://doi.org/10.1175/1520-
688 0469(1995)052%3C1959:ATDNRT%3E2.0.CO;2

689 McFarlane, N. A., 1987: The effect of orographically excited gravity wave drag on the general
690 circulation of the lower stratosphere and troposphere. *J. Atmos. Sci*, **44**, 1775–
691 1800, https://doi.org/10.1175/1520-0469(1987)044<1775:teooeg>2.0.co;2

692 Miranda, P. M. A., and I. N. James, 1992: Non-linear three-dimensional effects on the wave drag:
693 Splitting flow and breaking waves. *Quart. J. Roy. Meteor. Soc.*, **118**, 1057–1081.
694 https://doi.org/10.1002/qj.49711850803

695 Palmer, T. N., G. J. Shutts, and R. Swinbank, 1986: Alleviation of systematic westerly bias in
696 general circulation and numerical weather prediction models through an orographic gravity
697 wave drag parameterization. *Quart. J. Roy. Meteor. Soc.*, **112**, 1001–1039,
698 https://doi.org/10.1002/qj.49711247406

699 Phillips, D. S., 1984: Analytical surface pressure and drag for linear hydrostatic flow over three-
700 dimensional elliptical mountains. *J. Atmos. Sci.*, **41**, 1073–1084,
701 https://doi.org/10.1175/1520-0469(1984)041%3C1073:ASPADF%3E2.0.CO;2

702 Plougonven R., A. de la Cámara, A. Hertzog., and F. Lott, 2020: How does knowledge of
703 atmospheric gravity waves guide their parameterizations? *Quart. J. Roy. Meteor. Soc.*, **146**,
704 1529–1543, https://doi.org/10.1002/qj.3732

705 Pulido, M., and C. Rodas, 2011: A higher-order ray approximation applied to orographic waves:
706 Gaussian beam approximation. *J. Atmos. Sci.*, **68**, 46–60,
707 https://doi.org/10.1175/2010JAS3468.1

708 Scinocca, J. F., and N. A. McFarlane, 2000: The parametrization of drag induced by stratified flow
709 over anisotropic orography. *Quart. J. Roy. Meteor. Soc.*, **126**, 2353–2393,
710 https://doi.org/10.1002/qj.49712656802

711 Scorer, R. S., 1949: Theory of waves in the lee of mountains. *Quart. J. Roy. Meteor. Soc.*, **75**, 41–
712 56, https://doi.org/10.1002/qj.49707532308

713 Shutts, G., 1995: Gravity-wave drag parameterization over complex terrain: The effect of critical-
714 level absorption in directional wind-shear. *Quart. J. Roy. Meteor. Soc.*, **121**, 1005–1021,
715 https://doi.org/10.1002/qj.49712152504

716 Shutts, G. J., 1998: Stationary gravity-wave structure in flows with directional wind shear. *Quart.*
717 *J. Roy. Meteor. Soc.*, **124,** 1421–1442, https://doi.org/10.1002/qj.49712454905

718 Skamarock, W., J. B. Klemp, M. G. Duda, and coauthors, 2012: A multiscale nonhydrostatic
719 atmospheric model using centroidal voronoi tesselations and C-grid staggering. *Mon. Wea.*
720 *Rev.*, **140**, 3090–3105, https://doi.org/10.1175/MWR-D-11-00215.1

721 Smith, R. B., 1979: The influence of mountains on the atmosphere. Advances in Geophysics, **21**,
722 87–230, https://doi.org/10.1016/S0065-2687(08)60262-9

723 Smith, R. B., 1980. Linear theory of stratified flow past an isolated mountain. *Tellus*, **32**, 348–364.
724 https://doi.org/10.1111/j.2153-3490.1980.tb00962.x

725 Smith, R. B., 1985: On severe downslope winds. *J. Atmos. Sci*., **42**, 2597–2603,
726 https://doi.org/10.1175/1520-0469(1985)042%3C2597:OSDW%3E2.0.CO;2

727 Song, I.-S., and H.-Y. Chun, 2008: A Lagrangian spectral parameterization of gravity wave drag
728 induced by cumulus convection. *J. Atmos. Sci.*, **65,** 1204–1224,
729 https://doi.org/10.1175/2007JAS2369.1

730 Teixeira, M. A. C., and P. M. A. Miranda, 2006: A linear model of gravity wave drag for
731 hydrostatic sheared flow over elliptical mountains. *Quart. J. Roy. Meteor. Soc*., **132**, 2439–
732 2458. https://doi.org/10.1256/qj.05.220

733 Teixeira, M. A. C., and P. M. A. Miranda, 2009: On the momentum fluxes associated with
734 mountain waves in directionally sheared flows. *J. Atmos. Sci*., **66**, 3419–3433.
735 https://doi.org/ 10.1175/2009JAS3065.1

736 Teixeira, M. A. C., and C. L. Yu, 2014: The gravity wave momentum flux in hydrostatic flow with
737 directional shear over elliptical mountains. *Eur. J. Mech. Fluids*, 47B, 16–31,
738 https://doi.org/10.1016/j.euromechflu.2014.02.004.

739 Teixeira, M. A. C., P. M. A. Miranda, and R. M. Cardoso, 2008: Asymptotic gravity wave drag
740 expression for non-hydrostatic rotating flow over a ridge. *Quart. J. Roy. Meteor.*
741 *Soc*., **134**, 271–276. https://doi.org/10.1002/qj.196

742 Teixeira, M. A. C., P. M. A., Miranda, and M. A. Valente, 2004. An analytical model of mountain
743 wave drag for wind profiles with shear and curvature. *J. Atmos. Sci*., **61**, 1040–1054.
744 https://doi.org/10.1175/1520-0469(2004)061<1040:AAMOMW>2.0.CO;2

745 Turner, H. V., M. A. C. Teixeira, J. Methven, and S. B. Vosper, 2019: Sensitivity of the surface
746 orographic gravity wave drag to vertical wind shear over Antarctica. *Quart. J. Roy. Meteor.*
747 *Soc.*, **145**, 164-178. https://doi.org/10.1002/qj.3416

748 Wurtele, M. G., R. D. Sharman, and A. Datta, 1996: Atmospheric lee waves. *Ann. Rev. Fluid*
749 *Mech*., **28**, 429–476, https://doi.org/10.1146/annurev.fl.28.010196.002241

750 Xu, X., Y. Wang, and M. Xue, 2012: Momentum flux and flux divergence of gravity waves in
751 directional shear flows over three-dimensional mountains. *J. Atmos. Sci.*, **69,** 3733–3744,
752 https://doi.org/10.1175/JAS-D-12-044.1

753 Xu, X., J. Song, Y. Wang, and M. Xue, 2017a: Quantifying the effect of horizontal propagation of
754 three-dimensional mountain waves on the wave momentum flux using Gaussian Beam
755 Approximation. *J. Atmos. Sci*., **74**, 1783–1798, https://doi.org/10.1175/JAS-D-16-0275.1

756 Xu, X., S. Shu, and Y. Wang, 2017b: Another look on the structure of mountain waves: A spectral
757 perspective. *Atmos. Res*., **191**, 156–163, https://doi.org/10.1016/j.atmosres.2017.03.015

758 Xu, X., Y. Tang, Y. Wang, and M. Xue, 2018: Directional absorption of mountain waves and its
759 influence on the wave momentum transport in the Northern Hemisphere. *J. Geophy. Res.*
760 *Atmos.*, **123**, 2640-2654, https://doi.org/10.1002/2017JD027968

761 Xu, X., M. Xue, M. A. C. Teixeira, J. Tang, and Y. Wang, 2019: Parameterization of directional
762 absorption of orographic gravity waves and its impact on the atmospheric general

circulation simulated by the Weather Research and Forecasting model. *J. Atmos. Sci*., **76**, 3435−3453. https://doi.org/10.1175/JAS-D-18-0365.1

Xu, X., M. A. C. Teixeira, M. Xue, Y. Lu, and J. Tang, 2020: Impacts of wind profile shear and curvature on the parameterized orographic gravity wave stress in the Weather Research and Forecasting model. *Q. J. R. Meteorol. Soc.*, **146**, 3086-3100. https://doi.org/10.1002/qj.3828

Xue, M., and A. J. Thorpe, 1991: A mesoscale numerical model using the nonhydrostatic sigma-coordinate equations: Model experiments with dry mountain flows. *Mon. Wea. Rev*., **119**, 1168−1185, https://doi.org/10.1175/1520-0493(1991)119%3C1168:AMNMUT%3E2.0.CO;2

Xue, M., K. K. Droegemeier, and V. Wong, 2000: The Advanced Regional Prediction System (ARPS) – A multi-scale nonhydrostatic atmospheric simulation and prediction model. Part I: Model dynamics and verification. *Meteorol. Atmos. Phys*., **75**, 161–193

Zängl, G., 2003: Orographic gravity waves close to the nonhydrostatic limit of vertical propagation. *J. Atmos. Sci*., **60**, 2045−2063, https://doi.org/10.1175/1520-0469(2003)060%3C2045:OGWCTT%3E2.0.CO;2

Zhang, Y., J. Li, R. Yu, and coauthors, 2019: A layer-averaged nonhydrostatic dynamical framework on an unstructured mesh for global and regional atmospheric modeling: Model description, baseline evaluation, and sensitivity exploration. *J. Adv. Model. Earth Sy.*, **11**, 1685−1714, https://doi.org/10.1002/2017MS001088

783 Zhou, L., S.-J. Lin, J.-H. Chen, and coauthors, 2019: Toward convective-scale prediction within
784 the next generation global prediction system. *Bull. Amer. Meteor. Soc*., 100, 1225−1243,
785 https://doi.org/10.1175/BAMS-D-17-0246.1

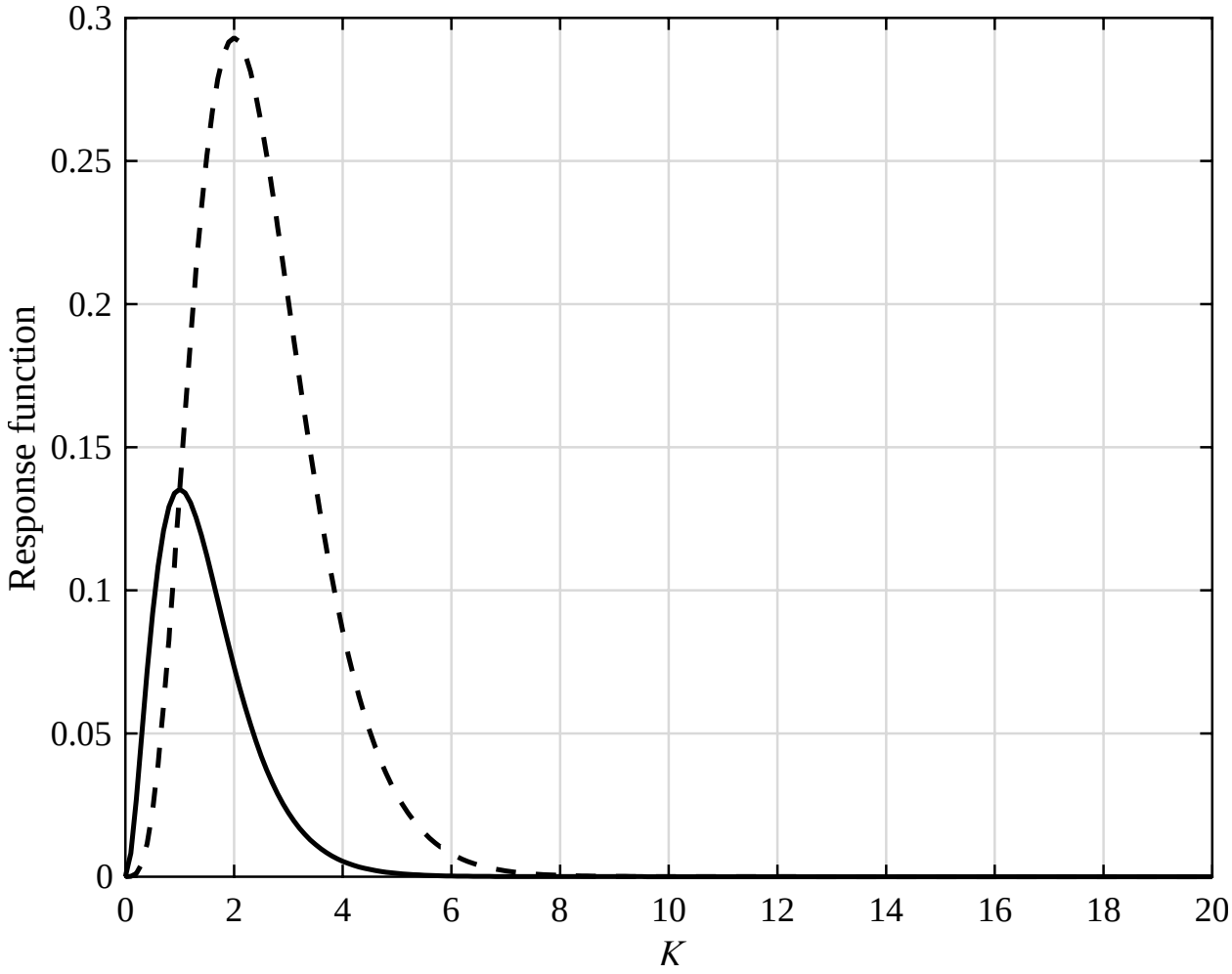

Fig. 1 Response functions $\widetilde{K}^2 e^{-2\widetilde{K}}$ (solid) and $\widetilde{K}^4 e^{-2\widetilde{K}}$ (dashed).

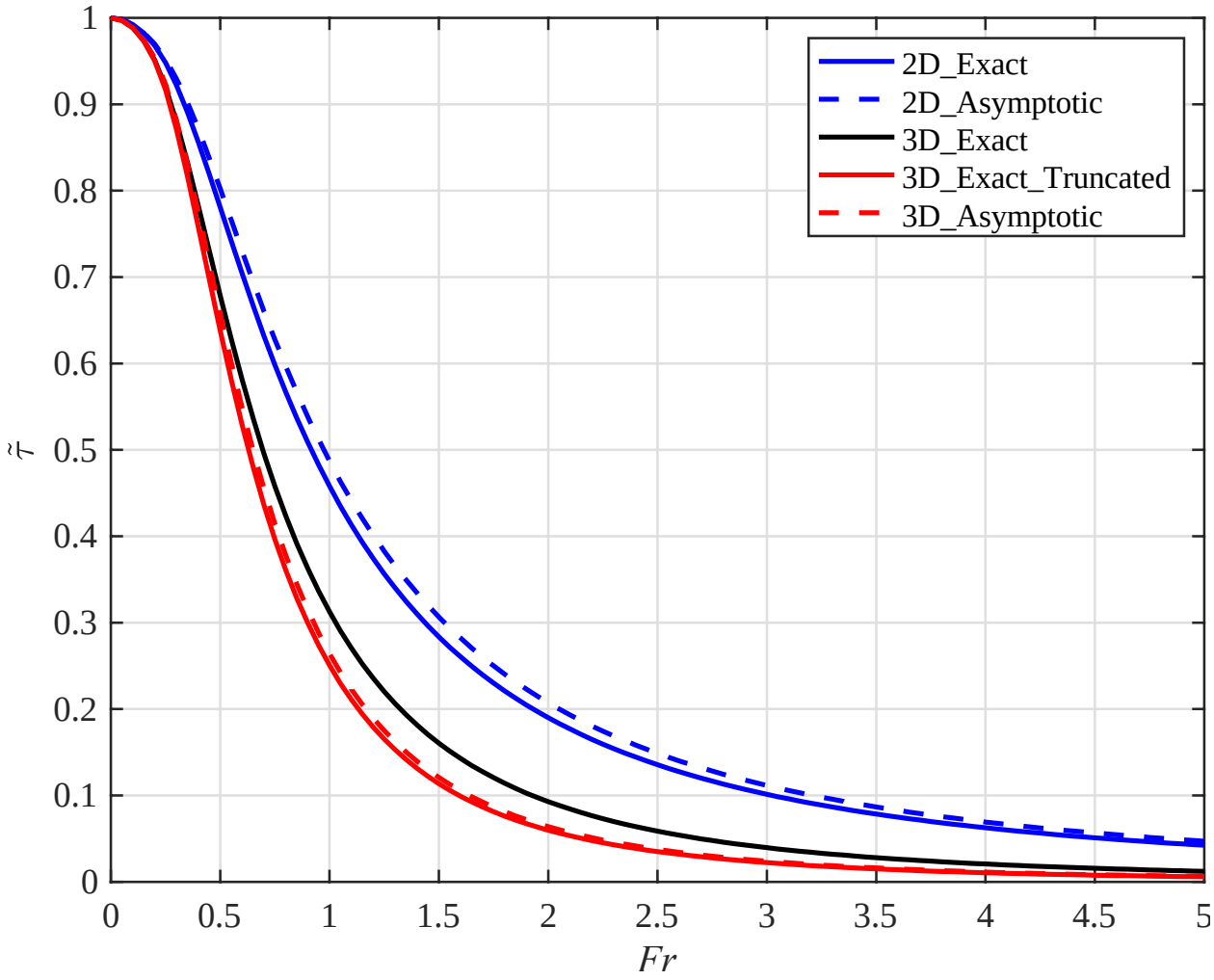

Fig. 2 Variation of the normalized GWMF ($\tilde{\tau}$) with the horizontal Froude number (Fr). Blue lines are for the nonhydrostatic OGWs forced by 2D bell-shaped ridges, while the black and red lines are for those forced by 3D circular bell-shaped mountains. The normalization is made with respect to their hydrostatic counterparts.

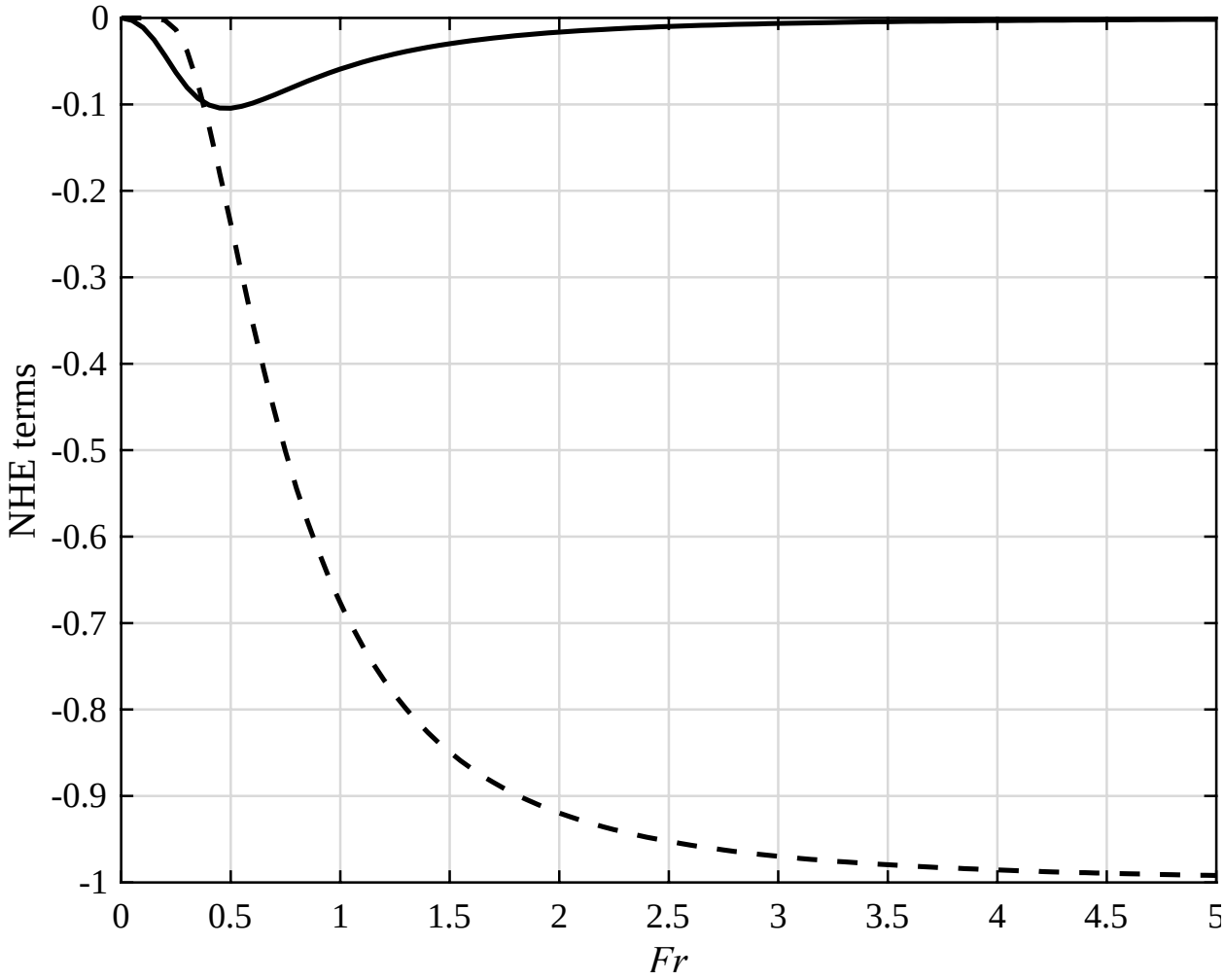

794

795 Fig. 3 Variations of the NHE1 (dashed) and NHE2 (solid) terms with the horizontal Froude number
796 (*Fr*) in the case of isotropic terrain.

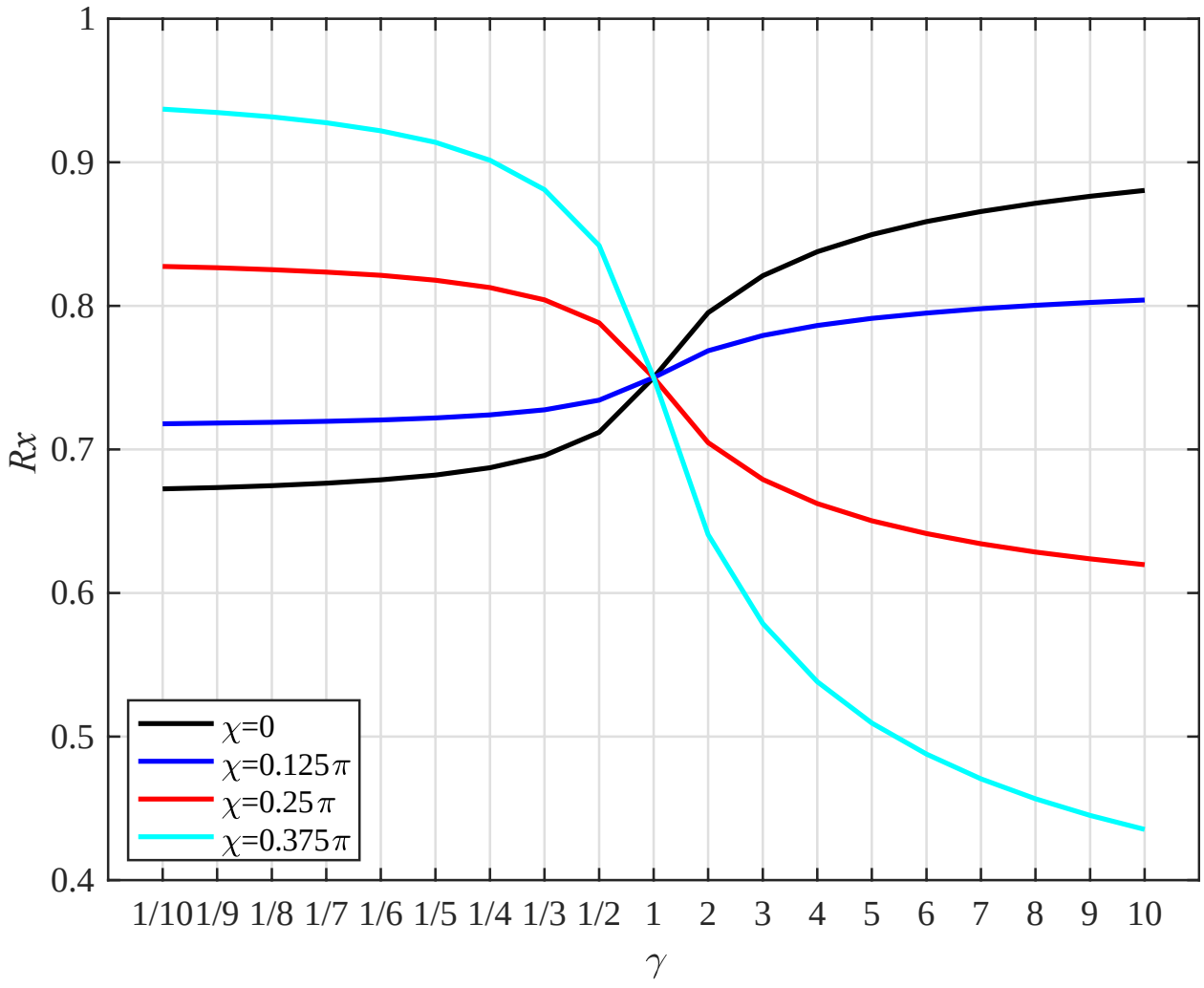

Fig. 4 Variation of $R_x(\gamma, \chi)$ as a function of terrain anisotropy (γ) for different horizontal wind directions (χ).

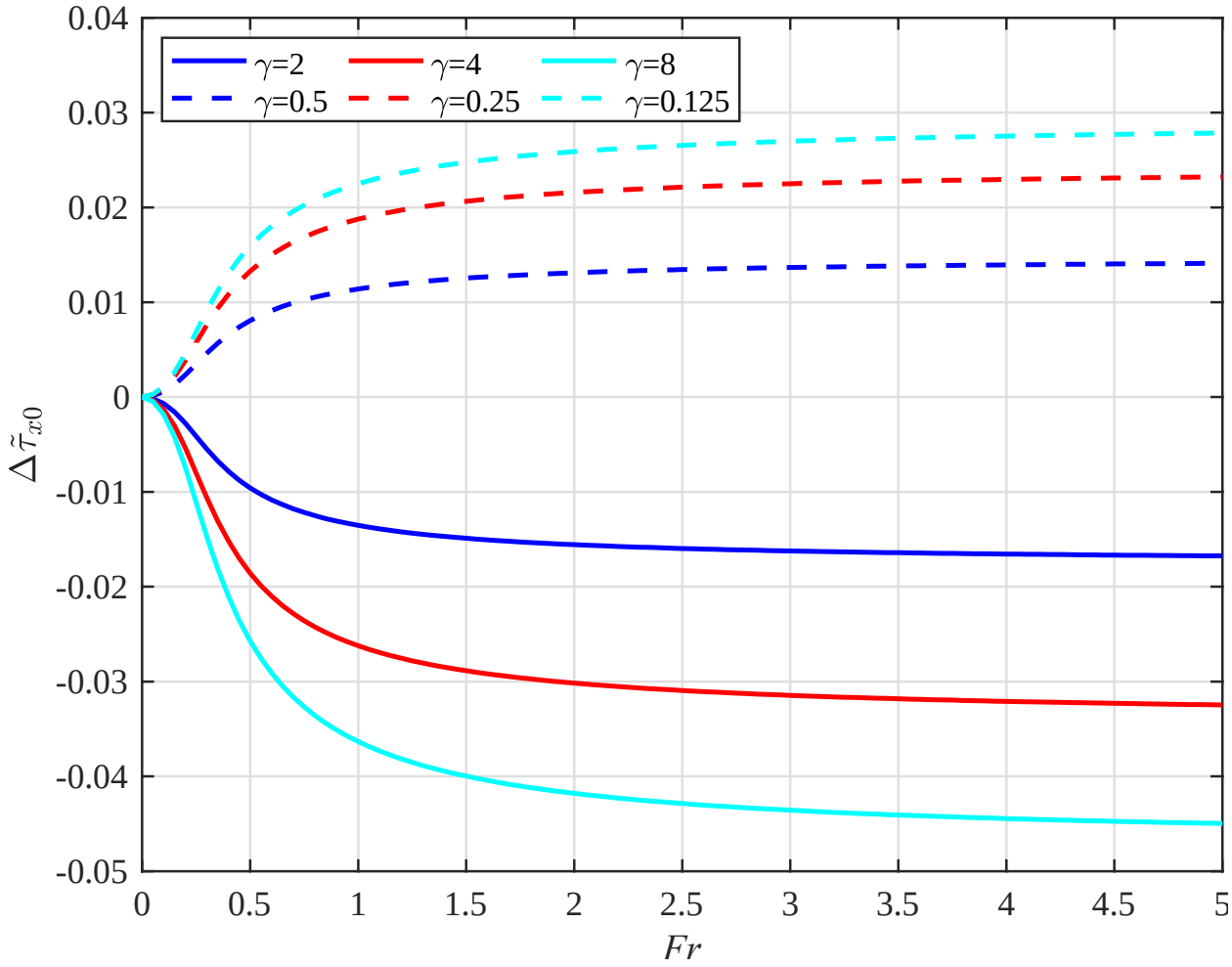

Fig. 5 Variation of $\Delta\tilde{\tau}_{x0}$ in the parallel-flow case as a function of horizontal Froude number (Fr) for different terrain anisotropies (γ).

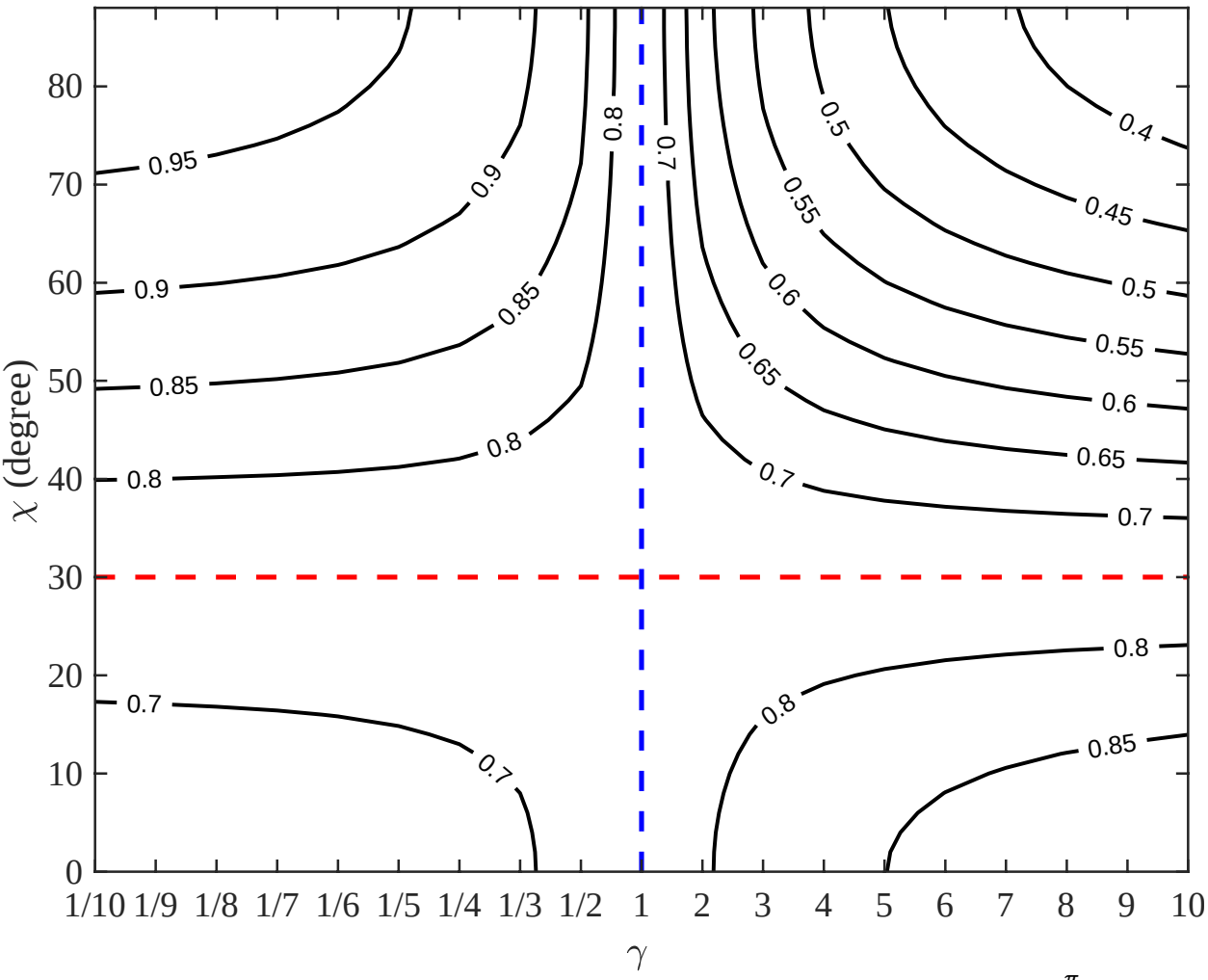

Fig. 6 Distribution of $R_x(\gamma, \chi)$ in γ- χ parameter space. The red line represents $\chi = \frac{\pi}{6}$ while the blue line indicates γ = 1.

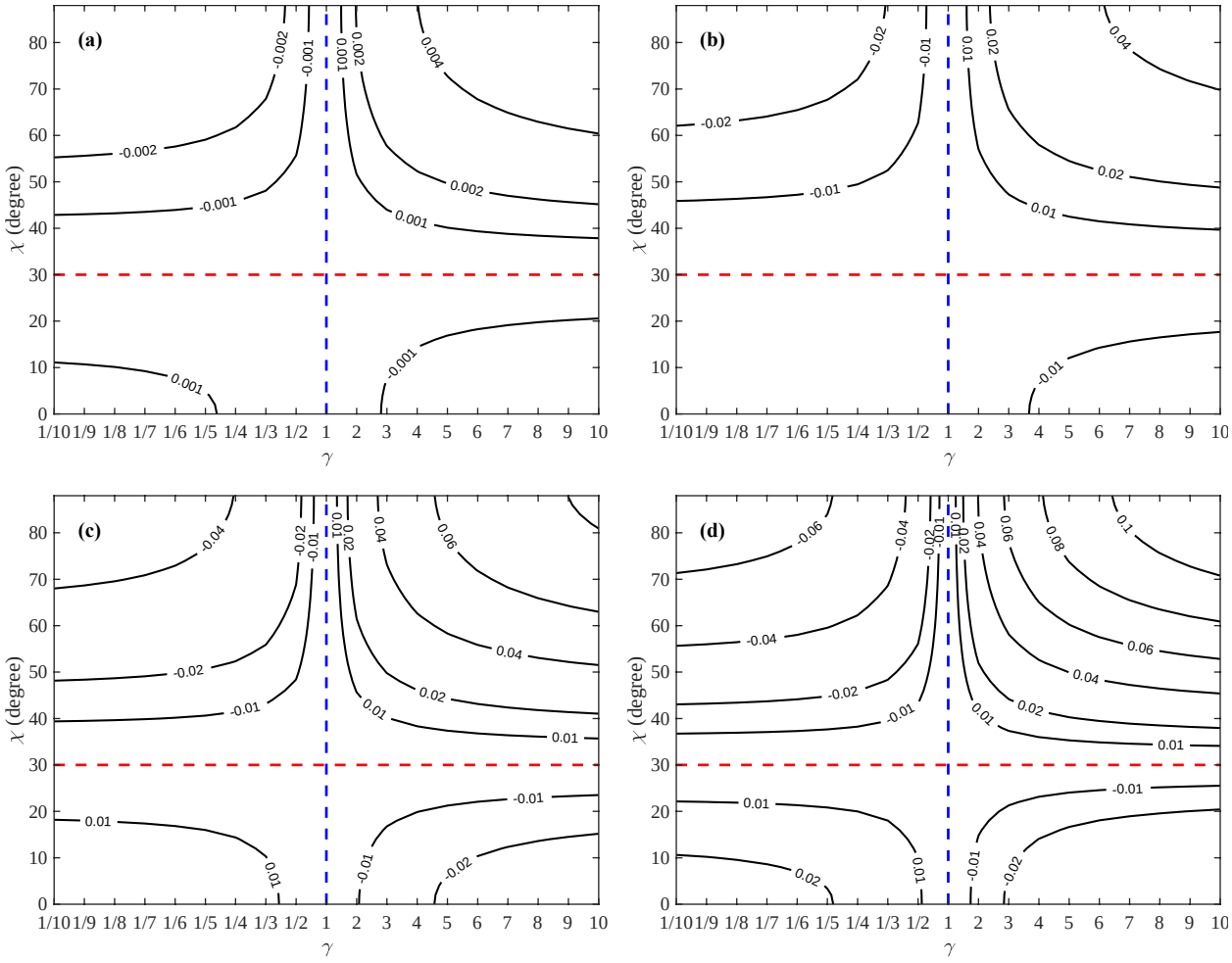

Fig. 7 Distribution of $\Delta\tilde{\tau}_x$ in γ- χ parameter space at different horizontal Froude numbers: (a) Fr = 0.1, (b) Fr = 0.3, (c) Fr = 0.5, and (d) Fr = 1.0. The red line represents $\chi = \frac{\pi}{6}$ while the blue line indicates γ = 1.

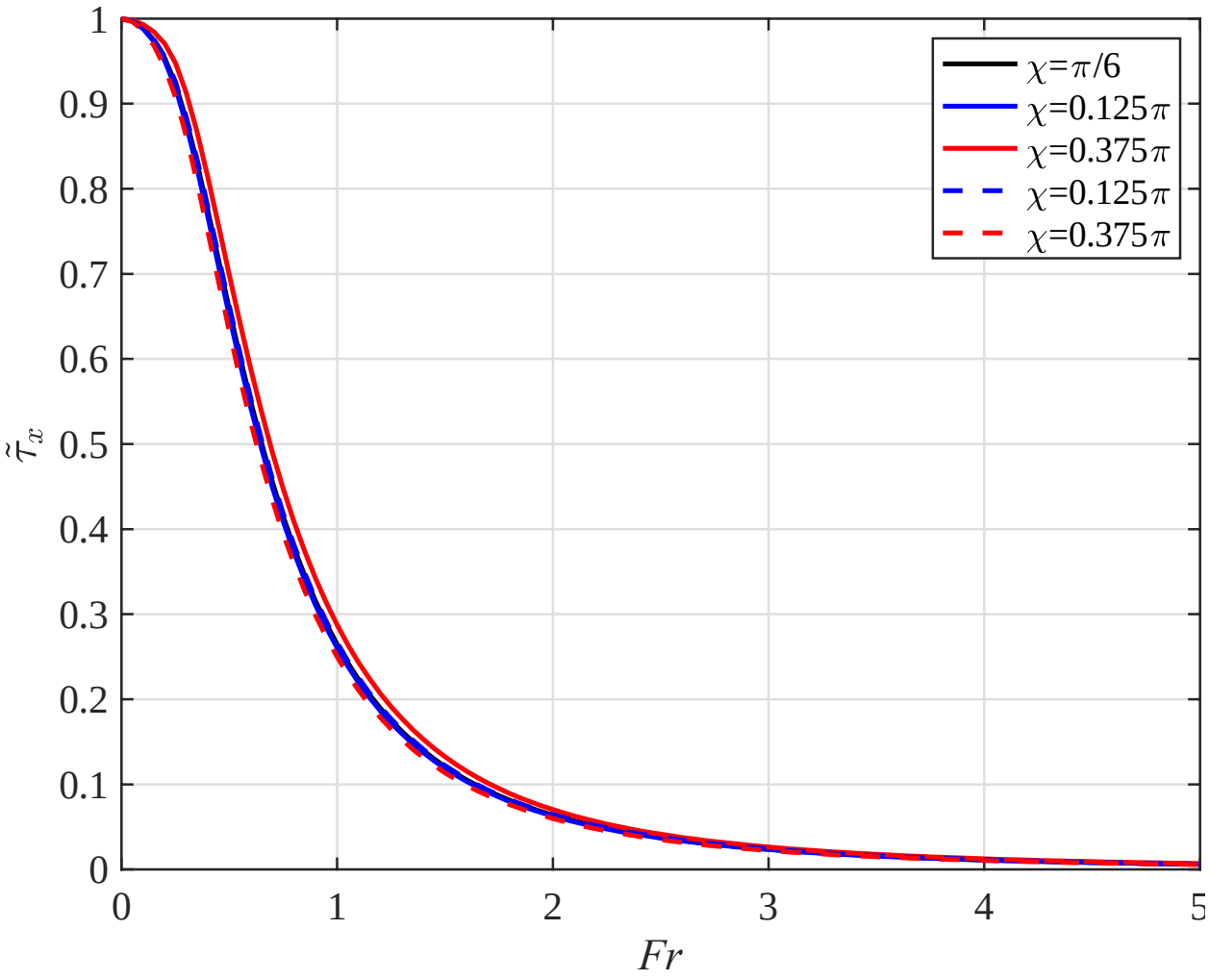

Fig. 8 Variation of the *x*-component of the normalized GWMF ($\tilde{\tau}_x$) in the oblique-flow case as a function of the horizontal Froude number (*Fr*). Solid and dashed lines are for $\gamma = 8$ and $\gamma = \frac{1}{8}$, respectively.

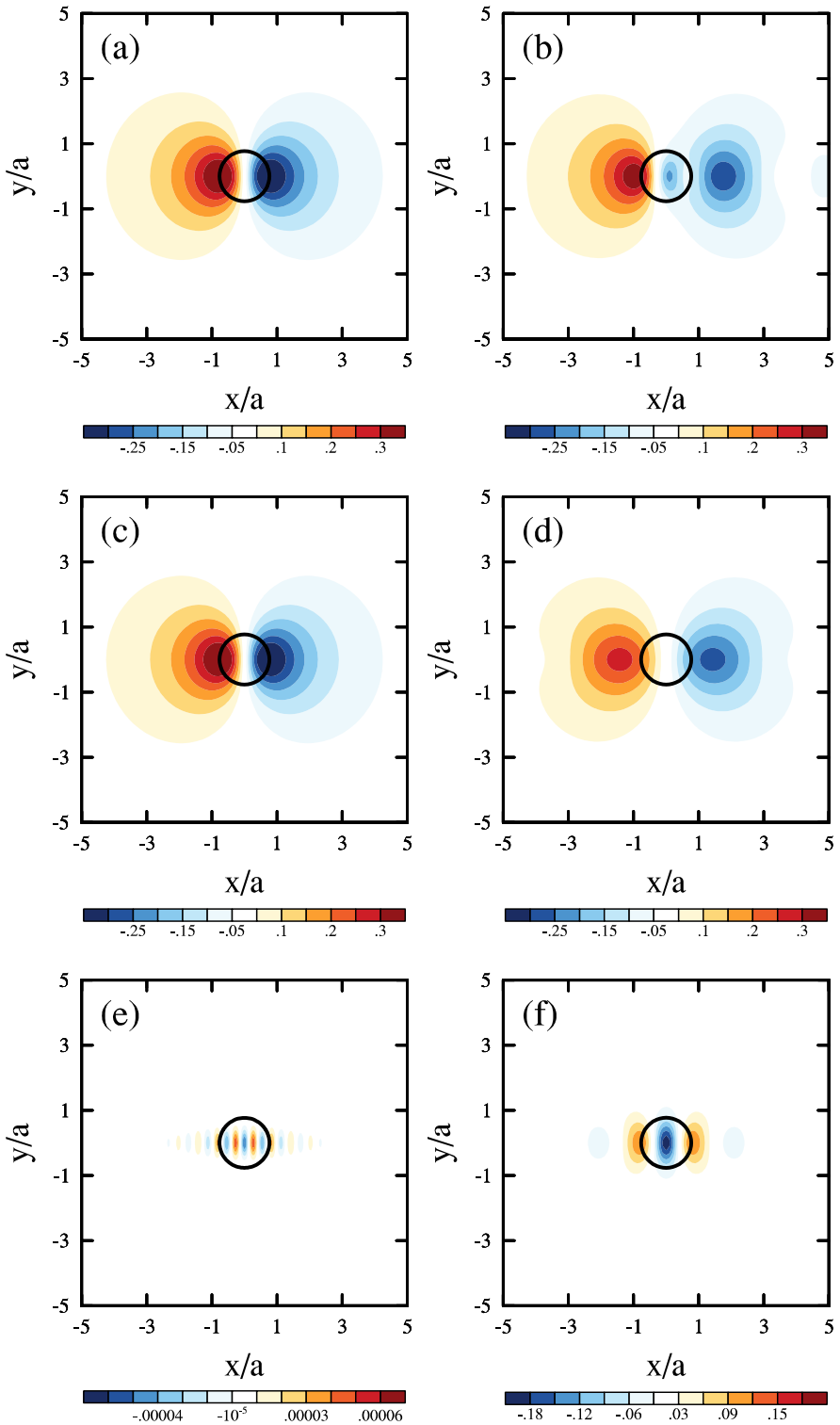

Fig. 9 Exact surface pressure perturbation (top) of nonhydrostatic OGWs forced by a circular bell-shaped mountain, which is the sum of p_{GW} (middle) and $p_{\text{evanescent}}$ (bottom). See appendix for details. (a) (c) and (e) are for Fr = 0.1, while (b) (d) and (f) are for Fr = 0.5. The pressure perturbations are scaled with $\bar{\rho}N\left|\widetilde{\mathbf{V}}\right|h_0$. The axes are scaled by the mountain half width a. The black circle indicates the contour of 0.5 h_0, with h_0 being the maximum elevation of the mountain.

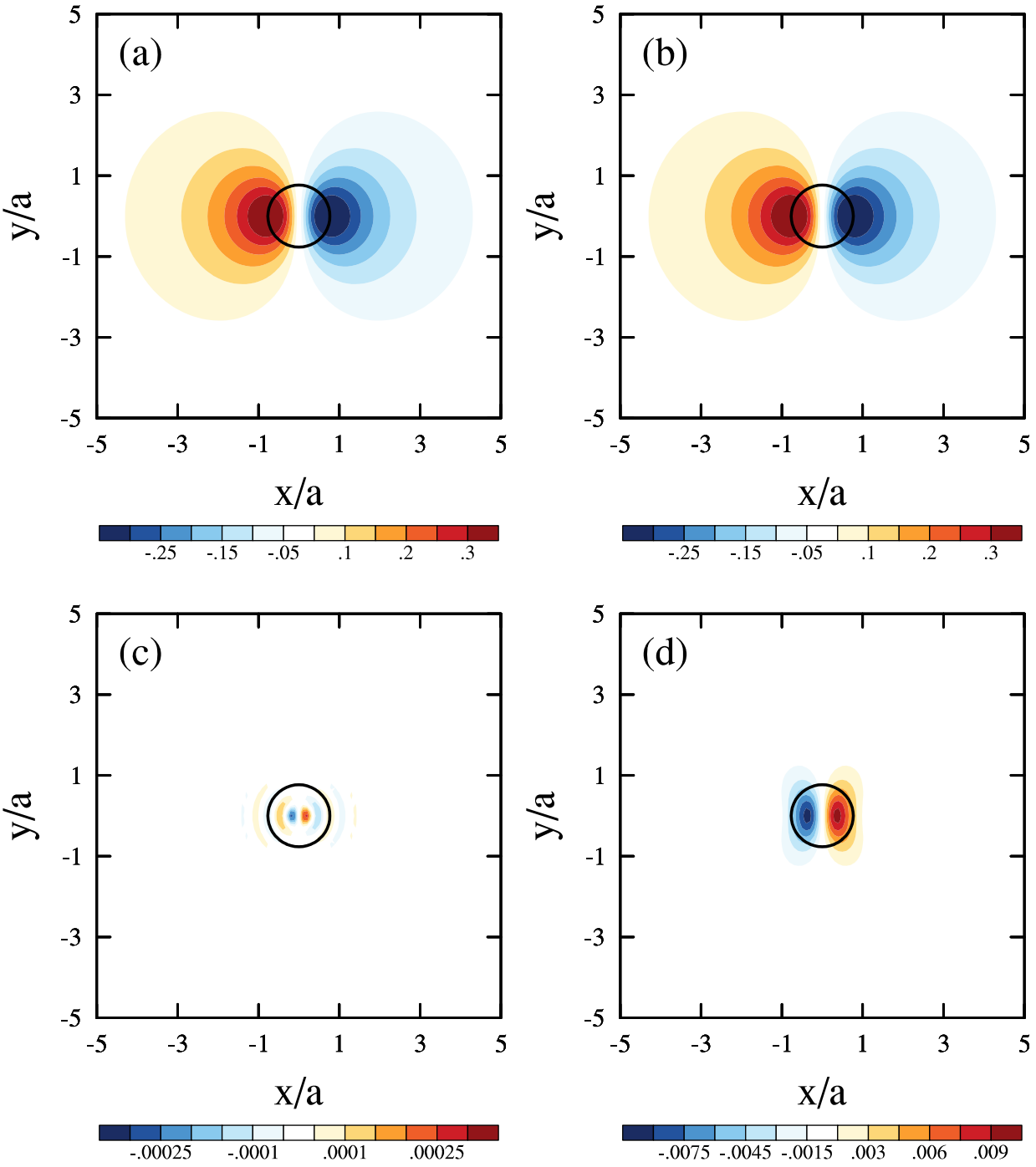

Fig. 10 (a) Asymptotic surface pressure perturbation of nonhydrostatic vertically propagating OGWs forced by a circular bell-shaped mountain at $Fr = 0.1$, which is the sum of (b) p_0, (c) p_1 and (d) p_2 (see appendix for details). The pressure perturbations are scaled with $\bar{\rho}N\left|\widetilde{\mathbf{V}}\right|h_0$. The axes are scaled by the mountain half width a. The black circle indicates the contour 0.5 h_0, with h_0 being the maximum elevation of the mountain.

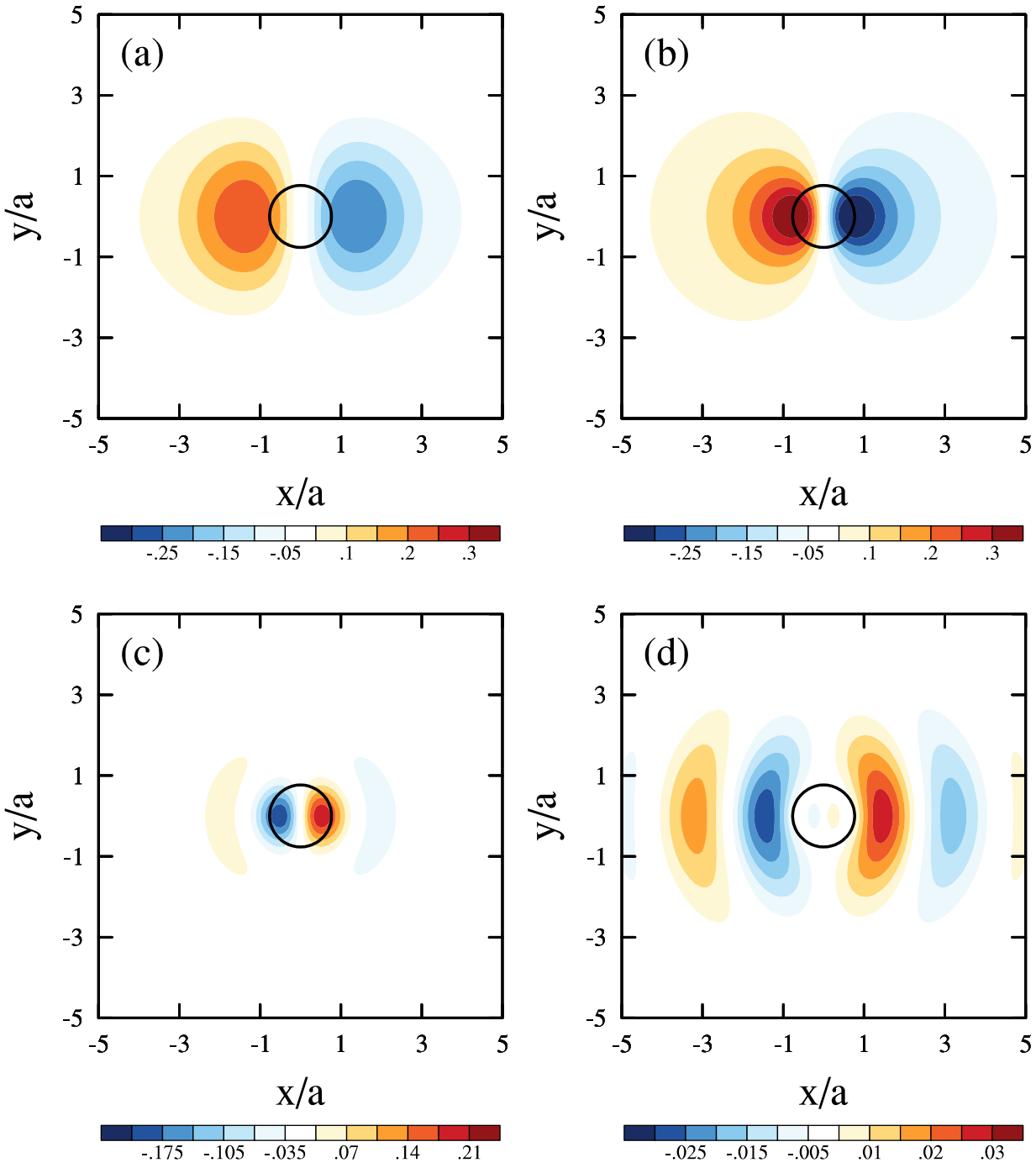

827

828 Fig. 11 Same as Fig. 10 but for *Fr* = 0.5.